Serpentinization and Magmatic Distribution in a Hyperextended Rift Suture: Implication for Natural Hydrogen Exploration (Mauléon Basin, Pyrenees)

Nicolas Saspiturry, Cécile Allanic, Aurélie Peyrefitte

Tectonics®

RESEARCH ARTICLE
10.1029/2024TC008385

Key Points:

- We address the distribution of serpentinization in an inverted hyperextended rift system based on joint gravimetric and magnetic modeling
- The mantle is gradually serpentinized on an overall thickness of around 15 km reaching a maximum amount of nearly 76%
- The mantle and the basement top are respectively in optimal thermal windows to generate H2 by serpentinization and trap it

Supporting Information:

Supporting Information may be found in the online version of this article.

Correspondence to:

N. Saspiturry,
nicolas.saspiturry@umontpellier.fr

Citation:

Saspiturry, N., Allanic, C., & Peyrefitte, A. (2024). Serpentinization and magmatic distribution in a hyperextended rift suture: Implication for natural hydrogen exploration (Mauléon basin, Pyrenees). *Tectonics*, *43*, e2024TC008385. https://doi.org/10.1029/2024TC008385

Received 19 APR 2024
Accepted 26 JUL 2024

Author Contributions:

Conceptualization: N. Saspiturry, C. Allanic
Data curation: A. Peyrefitte
Formal analysis: N. Saspiturry
Methodology: A. Peyrefitte
Resources: C. Allanic
Software: A. Peyrefitte
Validation: C. Allanic, A. Peyrefitte
Writing – original draft: N. Saspiturry
Writing – review & editing: C. Allanic, A. Peyrefitte

Serpentinization and Magmatic Distribution in a Hyperextended Rift Suture: Implication for Natural Hydrogen Exploration (Mauléon Basin, Pyrenees)

N. Saspiturry[1], C. Allanic[2], and A. Peyrefitte[2]

[1]Géosciences Montpellier, CNRS, University of Montpellier, Montpellier, France, [2]BRGM-French Geological Survey, Orléans, France

Abstract The Mauléon basin is a world-class example of hyperextended rift suture. The basin possesses key attributes of an optimal hydrogen target, namely mantle, at shallow depth with tectonic structures rooted into it. Natural H2 seepages have been recognized at the surface in the foothills. Yet distribution and quantification of serpentinization within the mantel piece representing the potential H2 source has not been addressed while this aspect is crucial to consider further exploration. We discuss these aspects using joint gravimetric and magnetic 2D forward modeling along two orthogonal transects. 2D forward modeling shows that serpentinization gradually increases from bottom (20 km depth) to top reaching a maximum amount of nearly 76% (8 km depth). The N-S transect evidence that serpentinization fronts are northward inclined, suggesting a N-S serpentinization gradient responsible for the long wavelength gravity and magnetic anomalies. This orientation matches that of detachment within the former hyperextended domain, which exhumed the mantle during the Cretaceous. The W-E transect shows that serpentinization also increase toward the east reaching its maximum amount against the Barlanès lithospheric structure. The latter also coincides with the main short wavelength magnetic anomaly recognized in the basin. Forward geophysical modeling reveals that this anomaly could be linked to the presence, at shallow depth, of an alkaline magmatic body or a shallower piece of highly serpentinized subcontinental mantle both attesting for the paroxysm of the Cretaceous rifting phase. Finally, we propose a conceptual model of the H2 life cycle in the Mauléon basin and discuss the implications for H2 exploration.

1. Introduction

Natural hydrogen (H2) is emerging as a promising possible source of energy for a future low-carbon society. However, our current knowledge of the generation, migration, consumption, and accumulation of natural hydrogen is limited. In the absence of any consensus on optimal exploration strategy or resource assessment, it is not yet possible to consider exploitation of this resource. As a prerequisite, it is essential to estimate the potential of natural hydrogen with a sufficient level of reliability to prefigure future uses. In recent decades, natural hydrogen seepages have been described in mid-oceanic ridges (Marcaillou et al., 2011; Welhan & Craig, 1979), in onshore ophiolitic complexes (Abrajano et al., 1988, 1990; Deville & Prinzhofer, 2016; Neal & Stanger, 1983), and in sedimentary basins in Russia (Larin et al., 2015), USA (Zgonnik et al., 2015), Mali (Prinzhofer et al., 2018), Brazil (Moretti et al., 2021; Prinzhofer et al., 2019) and France (Lefeuvre et al., 2021, 2022). Where ultramafic rocks are exposed to water at temperatures lower than 400°C, they inevitably undergo serpentinization reactions that form serpentine ± brucite ± talc ± magnetite, releasing substantial amounts of natural hydrogen (Cannat et al., 2010; Coveney et al., 1987; Klein et al., 2013). Among the numerous processes known to generate natural hydrogen, serpentinization is among the most efficient (Cannat et al., 2010; Coveney et al., 1987; Klein et al., 2009, 2013; McCollom & Bach, 2009). Serpentinized subcontinental mantle is known to be widely present beneath hyperextended rifts and passive margins, making these sites potential targets for natural hydrogen exploration (Boillot et al., 1987; Manatschal, 2004; Manatschal et al., 2006). By estimating the area of exhumed mantle from wide-angle seismic profiles at North Atlantic magma-poor margins, Liu et al. (2023) calculated that the accumulated H2 production could have been as high as ~8.6 × 1,012 metric tons prior to North Atlantic Ocean opening, thus highlighting the significance of H2 generation at magma-poor margins.

The Mauléon basin in the west Pyrenean realm represents an Early Cretaceous hyperextended rift that developed at the Iberia-Eurasia plate boundary (Asti et al., 2022; Jammes et al., 2009; Lagabrielle et al., 2020; Masini et al., 2014; Saspiturry, Razin, et al., 2019; Saspiturry, Allanic, et al., 2020) (Figure 1). Serpentinization occurred in mantle material exhumed at the seafloor, as evidenced in outcrops of tectonic slices in the easternmost part of

10.1029/2024TC008385

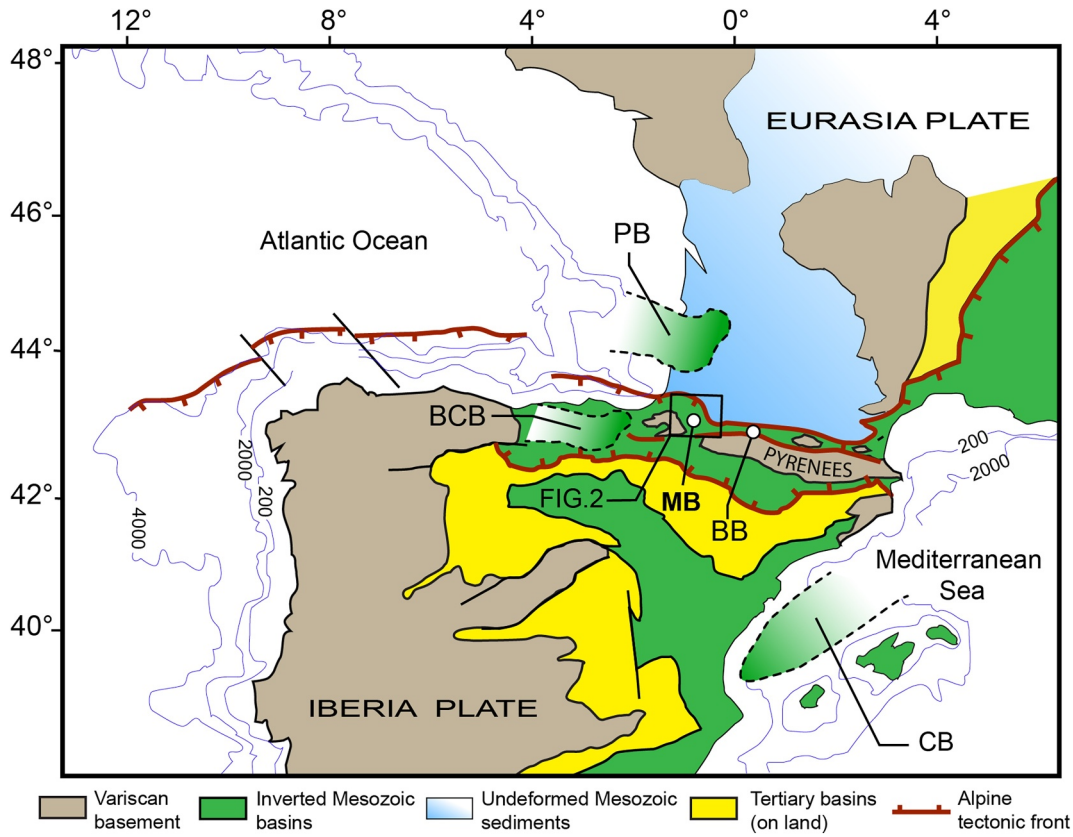

Figure 1. Structural map of the Cantabrian-Pyrenean orogenic system. PB: Parentis basin, BCB: Basque-Cantabrian basin, MB: Mauléon basin, BB: Baronnies basin, CB: Columbrets basin.

the basin (Fabriès et al., 1998; Lagabrielle, Asti, Fourcade, Corre, Poujol, et al., 2019; Lagabrielle, Asti, Fourcade, Corre, Uzel, 2019; Lagabrielle et al., 2020) (Urdach locality in Figure 2a). This domain subsequently underwent tectonic inversion, and serpentinized subcontinental mantle is supposed to remain preserved at shallow depth (~10 km) within the Mauléon basin pop-up (Lehujeur et al., 2021; Saspiturry et al., 2022; Wang et al., 2016) (Figure 2a). Indeed, the strong Labourd positive gravity anomaly (Casas et al., 1997; Grandjean, 1994), is localized upon a shallow high velocity body characterized by *P*-wave velocities of ~7.5–8 km/s in its core (Chevrot et al., 2018; Lehujeur et al., 2021; Wang et al., 2016). This anomaly is mainly localized in the western part of the Mauléon basin and ends on the Barlanès transfer zone (BTZ) (Figure 2b). However, the main magnetic anomaly recognized into the basin appears shifted from the Labourd gravimetric anomaly questioning their respective sources (Figure 2c).

The structural architecture of the Mauléon pop-up is controlled by the coeval development of N120° thrust systems and N20° syn-collisional transfer zones (Figure 2a; Saspiturry, Allanic, et al., 2020; Saspiturry et al., 2022). Both sets of structures root at depth in the high velocity body interpreted as subcontinental mantle (Lehujeur et al., 2021; Saspiturry et al., 2022; Wang et al., 2016). Thus, the Mauléon basin possesses three key attributes of a natural hydrogen exploration target: (a) serpentinized mantle (b) at shallow depth (c) with tectonic structures deeply rooted into it. Indeed, Lefeuvre et al. (2021, 2022) have documented several H2 hotspots in a soil-gas survey along major faults such as the North Pyrenean frontal thrust (NPFT) system (Figure 2d). They suggested that these structures represent potential pathways for natural hydrogen produced in the Mauléon basin mantle body. They also proposed that hydrogen could be trapped under salt diapirs in the hanging wall of the NPFT. However, our present knowledge of the Mauléon basin H2 source only comes down to the presence of a dense body with a high P-wave velocity, interpreted as sub-continental mantle. In this work we present joint gravimetric and magnetic forward 2D modeling along two orthogonal geological transects through the upper lithospheric structures of the Mauléon basin. This combined geological/geophysical approach allows to: (a) question the nature of the rocks behind the main gravimetric and magnetic anomalies recognized in the basin and

10.1029/2024TC008385

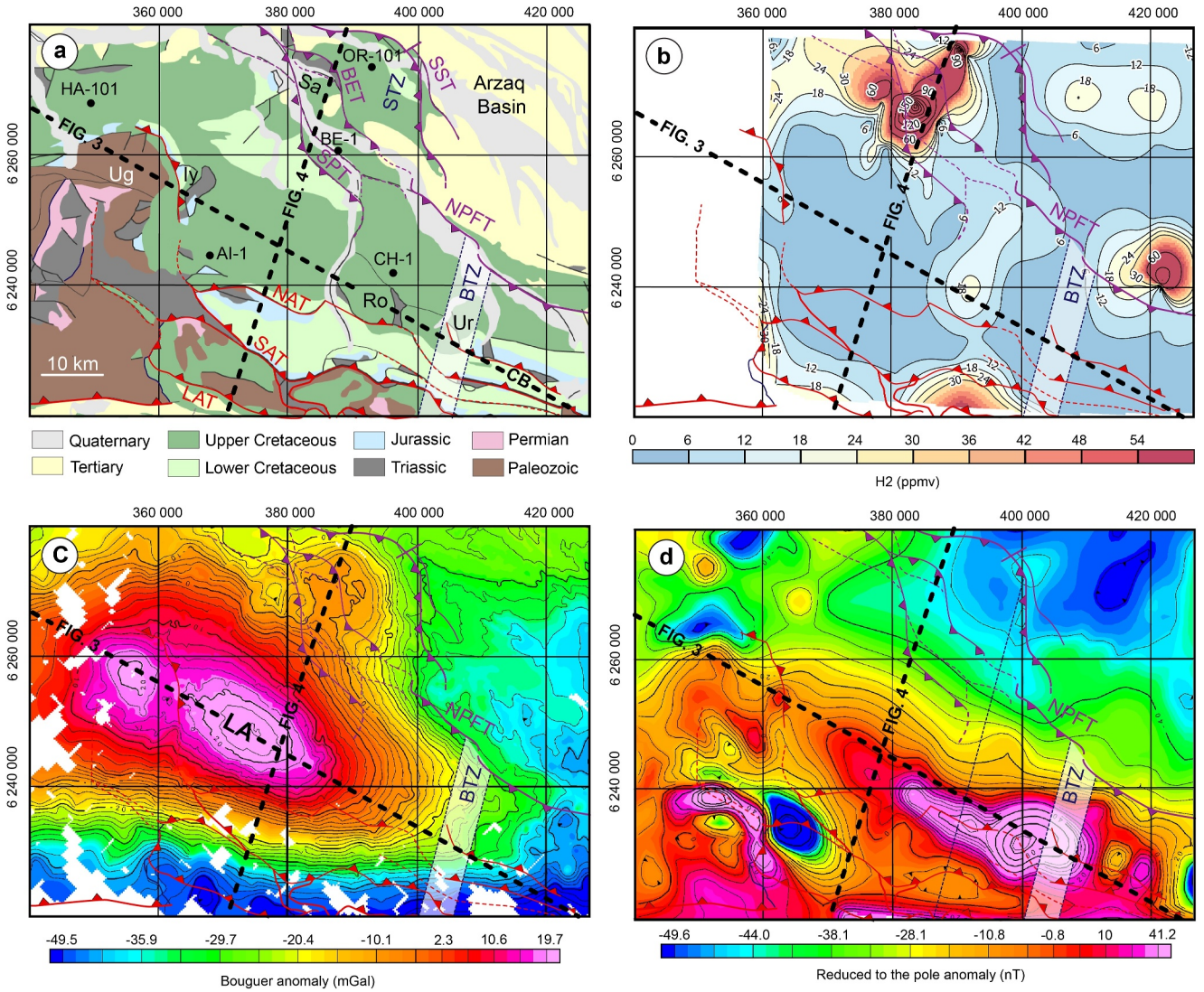

Figure 2. Geological, geophysical, and geochemical features of the Mauléon basin. Location in Figure 1. Black dashed lines are profiles for joint gravimetric and magnetic 2D forward modeling (Figures 3 and 4). (a) Bedrock and structural map highlighting the pop-up structure of the Mauléon basin with its flanking thrust faults (purple and red lines; teeth on upthrown side). Main north-vergent thrust faults (purple) are, from north to south, the Sainte-Suzanne thrust, North Pyrenean frontal thrust, Bellevue thrust, and Saint-Palais thrust. Main south-vergent thrust faults (red) are, from south to north, the Lakhoura thrust, South Arbailles thrust, and North Arbailles thrust. (b) Complete Bouguer anomaly map showing a strong positive anomaly centered upon the Mauléon basin. Contour interval, 10 mGal. (c) Reduced-to-the-pole anomaly map showing positive anomalies centered upon the Mauléon basin transfer zones. (d) Map of natural H2 seepages measured in the Mauléon basin (Lefeuvre et al., 2021). LA: Labourd gravity anomaly. CB: Chaînons béarnais. Transfer zones: ITZ Iholdy, STZ Saison, BTZ Barlanès. Drill holes: AI-1 Ainhice-1, OR-102 Orthez-102, BE-1 Bellevue-1, HA-101 Hasparren-101, CH-1 Chéraute-1. Salt diapirs: Sa Salies, Iy Iholdy, Ro Roquiague. Geologic features: Ug Ursuya granulites, Ur Urdach mantle body.

(b) address the distribution and amount of serpentinization within the mantle. Finally, these two geophysical transects offer new perspectives on: (a) the presence/absence of mantle in the optimum thermal window for generating H2 by serpentinization and (b) the identification of new potential H2 plays.

2. Geological Setting

The Pyrenean Mountain belt results from north-south convergence at the Iberian-Eurasian plate boundary from the Late Santonian to the Early Miocene (Angrand & Mouthereau, 2021; Olivet, 1996; Puigdefàbregas & Souquet, 1986; Rosenbaum et al., 2002). In its western part, the belt is made of four different structural units. To the north, the Aquitaine foreland basin is separated from the North Pyrenean Zone across the NPFT. To the south, the south verging Lakora thrust delimits the North Pyrenean Zone from the Axial Zone which corresponds to the

present-day high range of the Pyrenees. Finally, the South Pyrenean foreland basin is delimited from the Axial Zone by a set of south-verging thrusts. While the Axial Zone and the South Pyrenean foreland basin result from the antiformal nappe-stacking of the Early Cretaceous Iberian proximal rift margin, the North Pyrenean Zone consists in the shortening of the former Early Cretaceous necking zone and hyperextended rift domains (Labaume & Teixell, 2020; Masini et al., 2014; Saspiturry, Allanic, et al., 2020; Teixell et al., 2016; Tugend et al., 2014). In the north-western Pyrenees, the North Pyrenean Zone corresponds to the inverted Mauleon rift basin that is thrusted on top of the Aquitaine foreland basin by a set of north-verging thrust, namely from south to north: the Saint-Palais, Bellevue, and Sainte-Suzanne thrusts (Figure 2a; Daignières et al., 1994; Saspiturry, Razin, et al., 2019). At the front of the Sainte-Suzanne thrust, and buried underneath syn-orogenic sediments, the Arzacq basin corresponds to another Early-Cretaceous rift basin preserved from orogenic deformation (Figure 2a; Issautier et al., 2020). To the south, the inverted Iberian margin is affected by a set of south-verging thrusts, namely from north to south: the North Arbailles, South Arbailles and Lakora thrusts (Figure 2a; Saspiturry, Razin, et al., 2019; Saspiturry, Allanic, et al., 2020). The pre-orogenic rift template as well as the kinematics of rifting are still debated within the Mauleon and Arzacq basins. However, it is well established that these basins undergo continental crust thinning during the Early Cretaceous (Gomez-Romeu et al., 2019; Jammes et al., 2009; Labaume & Teixell, 2020; Lescoutre & Manatschal, 2020; Masini et al., 2014; Saspiturry, Razin, et al., 2019; Saspiturry, Allanic, et al., 2020; Teixell et al., 2016). These two basins are currently separated by a structural high, the Grand Rieu high, made of a thicker crustal block within the preserved early Cretaceous European proximal margin (Masini et al., 2014; Saspiturry, Razin, et al., 2019; Serrano et al., 2006). Although both basins underwent crustal thinning, the maximum rift intensity occurred within the Mauleon basin where local mantle exhumation associated with high temperature/low pressure metamorphism of the sedimentary cover occurred (Albarède & Michard-Vitrac, 1978; Lescoutre et al., 2019; Saspiturry, Lahfid, et al., 2020). Tectonic exhumation of mantle rocks was proposed to be accommodated by a set of N120° detachment faults (Gomez-Romeu et al., 2019; Jammes et al., 2009; Lescoutre et al., 2019; Masini et al., 2014; Saspiturry, Razin, et al., 2019; Saspiturry, Allanic, et al., 2020). However, final denudation of the mantle rocks seems to only occur along the Barlanès transverse structure. Indeed, intense extension was well demonstrated by the occurrence of deep crustal and mantle rocks material as clasts into the Urdach breccias interbedded within the late synrift turbiditic sequence in the vicinity of the BTZ (Debroas et al., 2010; Duée et al., 1984; Fortané et al., 1986; Jammes et al., 2009; Lagabrielle, Asti, Fourcade, Corre, Poujol, et al., 2019; Lagabrielle, Asti, Fourcade, Corre, Uzel, 2019; Roux, 1983; Saspiturry, Issautier, Razin, Andrieu, et al., 2021). Such observations show that these rocks were exposed at the seafloor before the onset of orogenesis. Although the basin does not reach the stage of oceanic accretion, it is characterized, in its easternmost part, by the development of postrift alkaline magmatism (Azambre & Rossy, 1976; Azambre et al., 1992; Thiébaut et al., 1979). The relics of this significant Cretaceous rifting stage are still visible today. Indeed, the western part of the Mauléon basin coincides with the large positive Labourd gravity anomaly, which is bounded to the east by the BTZ. Although this anomaly was initially attributed to the presence of lower crustal rocks at shallow depth (Grandjean, 1994; Pedreira et al., 2007; Vacher & Souriau, 2001), it has also been interpreted as a shallow piece of dense lithospheric mantle (Casas et al., 1997; Jammes et al., 2010). This interpretation has gained support from recent works documenting *P*-wave velocities of more than 7.3 km/s in this deep material (Chevrot et al., 2018; Lehujeur et al., 2021; Wang et al., 2016). The two geophysical modeled transects presented in this work will brings crucial information on the nature of the high velocity body localized under the Mauléon basin.

3. Data and Methodology

3.1. Gravimetric and Magnetic Data

Our area of interest is covered by gravity surveys archived in the Banque Gravimétrique de la France (Martelet et al., 2009). This data set totals 8,975 measurement points aligned with the IGSN71-Hayford 1930 gravity reference system. Classical gravity data reduction was performed to compute the complete Bouguer anomaly, including free-air and Bouguer corrections. For Bouguer slab reduction and terrain corrections, we chose a reference density of 2.6 g/cm^3, considering the orogenic geological context. Free air and Bouguer corrections were made using the IGN digital terrain model topographic data set (250 m resolution). Terrain corrections were computed for radii from 200 m to 10 km around the gravity stations, using the topographic grid resampled every 200 m, and from 10 to 167 km using topographic grids resampled at 1 km intervals (Martelet et al., 2002). The complete Bouguer anomaly map (Figure 2b) is interpretable in term of density contrasts below the topography.

The complete Bouguer anomaly map ranges from −60 to +25 mGal. Our study area is also covered by the New Magnetic compilation of the Bay of Biscay and surrounding continental shelves (Le Maire et al., 2021), which brings together all airborne magnetic data set available in our area of interest. Authors produced the magnetic anomaly map and the reduced-to-the-pole (RTP) magnetic anomaly map, both computed at 500 m and 3,000 m height. For the joint gravimetric and magnetic forward modeling, we used the RTP magnetic anomaly map computed at 500 m height, which relocates magnetic anomalies above their sources. The RTP magnetic anomaly field ranges from −96 to 111 nT.

3.2. 2D Geophysical Modeling

The complete Bouguer anomaly map (Figure 2b) and the RTP magnetic anomaly map (Figure 2c) were used as the observed geophysical data in our joint forward modeling. Only induced magnetization is considered for modeling. Gravimetric and magnetic processing and modeling were done using Oasis Montaj software. Gravimetric and magnetic direct modeling consists of simulating the distributions of density and magnetic susceptibility that best fit the observed geophysical data. The first step consists of positioning the profiles to be modeled and sampling the geophysical data along them. Next, a starting 2D geological model is created. It assigns values of density and magnetic susceptibility to each layer to allow the computation of gravimetric and magnetic response generated by the model. Modeling proceeds by modifying the geometry of the starting model to minimize the differences between the model output and the observed data. The wavelengths, intensity and shape of gravimetric and magnetic anomalies yield information about the depth and size of geological bodies who generate them. Joint modeling of magnetic and gravimetric signals allows a better understanding of the different sources to be modeled and increases the robustness of the results. Because magnetic and gravimetric methods yield nonunique solutions, different structures and bodies can equally well explain the observed signal. Therefore, knowledge of the geological context is essential for testing hypotheses and introducing constraints that reduce the inherent uncertainty of the method. The next section provides some information on the significant amount of data supporting the models presented in this paper (boreholes, seismic reflection profiles, passive seismic acquisitions, crustal balanced cross-sections).

3.3. Data Supporting the Models and Hypotheses To Be Tested

The spatial position of the modeled cross-sections was chosen to intersect the main gravity and magnetic anomalies recognized on the Mauléon basin (Figures 2b and 2c). They have been calibrated by numerous data some of which are presented in Figure S1 in Supporting Information S1. The north-south section follows the crustal-scale balanced cross-section published by Saspiturry, Allanic, et al. (2020) (Figure S1A in Supporting Information S1). *P*-wave velocity (V_p) lithospheric model constructed by full-waveform inversion allowed to constrain the lithospheric part of the north-south section (Figure S1A in Supporting Information S1; Wang et al., 2016) while the sedimentary pile as well as the basement top, has been calibrated thanks to a composite seismic reflection profile (lines MT104, MT112, and 83HBS02) (Figure S1B in Supporting Information S1; Saspiturry, Razin, et al., 2019). On this section, the Iberian antiformal nappe-stack (Pyrenean Axial Zone) is cropping in the southern part of the basin (Ducasse & Vélasque, 1988; Saspiturry, Razin, et al., 2019). The quasi-entire sedimentary pile has also been drilled. Indeed, this section is also calibrated by four boreholes, from south to north: Ainhice-1 (3,540.85 m depth); Uhart-Mixe-1 (1,868.8 m depth); Bellevue-1 (6,909 m depth), and Orthez-102 (5,489.10 m depth) (all these data are available in Saspiturry, Razin, et al., 2019). Only the Ainhice-1 borehole reaches the Paleozoic basement of the Mauléon Basin (Figure S1B in Supporting Information S1). The West-East cross section follows exactly the *P*-wave velocity (V_p) lithospheric model constructed by full-waveform inversion published by Saspiturry et al. (2022) allowing to constrain the lithospheric part of the section (Figure S1C in Supporting Information S1). The basement top and the sedimentary cover are partly calibrated in between the Iholdy and Barlanès transverse structures thank to a composite seismic reflexion profile available in Saspiturry et al. (2022) (lines MT116 and 82BAA12). This section is also calibrated by two boreholes, from west to east: Hasparren-101 (6,250 m depth) and Chéraute-1 (6,050 m depth) (all these data are available in Saspiturry, Lahfid, et al., 2020). On both sections, the Moho, the basement top, and the sedimentary cover have been calibrated using the 3D Maupassacq passive seismic acquisition (Lehujeur et al., 2021). The west-east section displays some early cretaceous diapirs reactivated during the Pyrenean compression. They are both visible at the outcrop and seismic scales. To the west of the BTZ, salt tectonic is recognized within the Iholdy and

Table 1
Parameter Values Used for the Modeling Hypotheses

Models			Density (g/cm^3)	Susceptibility (SI)	MAG	GRAVI
North-South	1A	Uniformly serpentinized mantle	2,900	0.0100	✗	✓
	1B	Serpentinized mantle with a petrophysical gradient of serpentinization increasing from bottom to top	2,700	0.06	✓	✓
			2,750	0.05		
			2,800	0.04		
			2,850	0.03		
			3,000	0.0020		
			3,100	0.0010		
			3,200	0.0005		
			3,300	0.0000		
West-East	2A	Uniformly serpentinized mantle	1A	1A	✗	✓
	2B	Gradient of serpentinization increasing from bottom to top	1B	1B	✗	✓
	3A	Uniformly serpentinized mantle—shallow mantle against the Barlanès transfer zone	1A	1A	✗	✗
	3B	Gradient of serpentinization increasing from bottom to top—shallow mantle against the Barlanès transfer zone	1B	1B	✓	✓
	4A	Uniformly serpentinized mantle—shallow alkaline magmatism against BTZ	Mantle: 1A	Mantle: 1A	✗	✗
			Magmatism: 2,900	Magmatism: 0.05		
	4B	Gradient of serpentinization increasing from bottom to top—shallow alkaline magmatism against BTZ	Mantle: 1B	Mantle: 1B	✓	✓
			Magmatism: 2,900	Magmatism: 0.05		

Note. Green arrow: very well adjusted; Red arrow: poorly adjusted. BTZ: Barlanès transfer zone. MAG: Modeled magnetic signal. GRAVI: Modeled gravimetric signal.

Roquiague diapirs (Canérot, 1988, 1989; Canérot et al., 2005; Saspiturry et al., 2022) while to the east, it is materialized by the Chaînons béarnais (CB) thrust welds and mini basins (Labaume & Teixell, 2020).

The complete Bouguer anomaly map displays a large positive anomaly, named the Labourd anomaly (Figure 2b). The anomaly is oriented WNW-ESE and is separated into two maxima. One of the working hypotheses tested and discussed in the results section consists of determining whether these maxima are linked to different sources or to the same sources which would be segmented by N20° transverse structures. Among the potential candidates to be at the origin of this anomaly, there are the Ursuya granulites (UrG) which outcrop in the westernmost part of the basin (Saspiturry, Cochelin, et al., 2019) and the subcontinental mantle imaged at around 10 km depth by passive seismic data (Lehujeur et al., 2021; Saspiturry et al., 2022; Wang et al., 2016). Some mantle slices corresponding to remnant bodies of the early cretaceous hyperextension are known at the outcrop scale, the Urdach body localized on the Barlanès structure and the Saraillé, Tos de la Coustette and Turon de la Técouère bodies localized on the CB segment (Figure 2b) (Corre et al., 2016; Fabriès et al., 1991, 1998; Labaume & Teixell, 2020; Lagabrielle, Asti, Fourcade, Corre, Poujol, et al., 2019, 2020). The RTP magnetic anomaly field features a WNW-ESE large positive anomaly at the eastern part of the basin (+111 nT) (Figure 2c). The two main magnetic and gravity anomalies therefore have the same orientation (WNW-ESE) but are shifted with respect to each other (Figures 2b and 2c). Another working hypotheses is therefore to test if these anomalies are generated by the same source. Eight geological models were produced to test their impact on the gravity and magnetic signal (Table 1). These models have the same petrophysical characteristics for the sedimentary cover and the continental crust. However, they differ in the distribution and amount of serpentinization: (a) uniformly serpentinized (models 1A, 2A, 3A, and 4A, Table 1) versus (b) gradually serpentinized (models 1B, 2B, 3B, and 4B, Table 1). The west-east models also differ in the presence or absence of heterogeneity at shallow depth against the BTZ: (a) mantle slice (models 3A and 3B; Table 1) versus (b) alkaline magmatic body (models 4A and 4B; Table 1).

3.4. Rock Density and Magnetic Susceptibility Calibration

3.4.1. Jurassic to Cenozoic Sedimentary Pile

To calibrate the gravimetric forward modeling of the sedimentary cover, we used a compilation of rock density values available in the vicinity of the Iberia-Eurasia plate boundary; the: North Pyrenean Zone (Torné

et al., 1989), Basque-Cantabrian basin (García-Senz et al., 2020; Pedreira et al., 2007), Mauléon basin (García-Senz et al., 2020; Grandjean, 1994; Martin et al., 2017; Vacher & Souriau, 2001; Wehr et al., 2018), Ebro basin (Pedreira et al., 2007; Pueyo et al., 2015; Torné et al., 1989), Aquitaine basin (Torné et al., 1989; Vacher & Souriau, 2001), and South Pyrenean Zone (Torné et al., 1989) (see compilation available in Table S1 in Supporting Information S1). Thus, the following rock densities were assigned according to previous published work: 2.60 g/cm^3 for Jurassic to Aptian carbonate rocks, 2.40 g/cm^3 for the lower part of the Cretaceous to Cenozoic sedimentary pile and 2.20 g/cm^3 for the upper part. Since, the sedimentary series do not contain magnetic material, a magnetic susceptibility of 0 SI was assigned to them.

3.4.2. Upper Triassic

The upper Triassic is composed of a wide range of rocks, that is, shale, evaporite and alkaline magmatic rock regionally named "ophites" (Curnelle, 1983; Lucas, 1985; Rossi et al., 2003). This unit is also widely involved in halokinetic deformation, associated with the Cretaceous rifting as well as the Pyrenean compression (Canérot, 1988, 1989; Canérot & Lenoble, 1993; Canérot et al., 2005; James & Canérot, 1999; Labaume & Teixell, 2020). The upper Triassic series are currently mainly composed of shale and alkaline magmatic rocks in the core of diapirs as the evaporites were dissolved during diapirs growth (Canérot et al., 2005; Labaume & Teixell, 2020). Thus, to take these heterogeneities into account as best as possible, two units were defined for the upper Triassic: a first unit dominated by evaporites and a second one mainly composed of alkaline magmatic rocks and shales. According to the regional data listed in Table S1 in Supporting Information S1 (García-Senz et al., 2020; Pedreira et al., 2007; Pueyo et al., 2015), a rock density of 2.20 g/cm^3 and a magnetic susceptibility of 0 SI has been attributed to the first upper Triassic salt-dominated unit. The second unit has been modeled with a rock density of 2.50 g/cm^3 and a magnetic susceptibility of 0.007 SI since it's dominated by ophites, and shales.

3.4.3. Continental Crust

To calibrate the gravimetric forward modeling of the continental crust, we used the wide regional data set listed in Table S1 in Supporting Information S1 (García-Senz et al., 2020; Grandjean, 1994; Martin et al., 2017; Neres et al., 2018; Pedreira et al., 2007; Pueyo et al., 2015; Torné et al., 1989; Vacher & Souriau, 2001; Wehr et al., 2018). The values used in our models also consider the fact that recent regional studies revealed that the Iberian crust is less dense than the European one (Wehr et al., 2018). Thus, for gravimetric modeling of continental crust, we used density values of 2.8 g/cm^3 (lower crust) to 2.7 g/cm^3 (upper crust) for Iberia and 2.9 g/cm^3 (lower crust) to 2.8 g/cm^3 (upper crust) for Europe. On the north -south profile, the uppermost part of the Axial Zone, mainly composed of metasediments (Saspiturry, Razin, et al., 2019), has been modeled with a rock density of 2.4 g/cm^3. On the west-east profile, the uppermost part of the UrG, widely altered by weathering (Saspiturry, Cochelin, et al., 2019), has also been modeled with a rock density of 2.4 g/cm^3. For magnetic modeling of continental crust, we used magnetic susceptibility values of 0.008 SI for the Iberian lower crust; 0.004 SI for the Iberian upper crust; 0.01 SI for the European lower crust and 0.005 to 0.001 SI for the European upper crust based on Pedreira et al. (2007) in the Basco-cantabric basin (upper crust: 0.001 SI; middle crust: 0.0035 SI; lower crust: 0.007 SI) and Neres et al. (2018) in the SW Iberian margin (upper crust: 0.005 Si; lower crust: 0.01 SI).

3.4.4. Alkaline Magmatism

The hypothesis of an alkaline magmatic intrusion in the vicinity of the BTZ (models 4A and 4B; Table 1) has been tested with a rock density of 2.9 g/cm^3 and a magnetic susceptibility of 0.05 SI. These values are consistent with rock density of 2.7–3 g/cm^3 and magnetic susceptibly of 0.04–0.06 SI reported for similar magmatic intrusion in the Gulf of Lion (Canva et al., 2019), the Bilbao synclinorium (Pedreira et al., 2007), the Lusitanian Basin (Neres et al., 2012, 2014), the Sines massif (Ribeiro et al., 2013) or the Portimão and the Guadalquivir Banks in the ocean-continent transition of the SW Iberia margin (Neres et al., 2018).

3.4.5. Sub-Continental Mantle

Serpentinization process induces the linear decrease of mantle rock density (Bina & Henry, 1990; Christensen, 1978; Krammer, 1990; Nazarova, 1994; Oufi et al., 2002; Toft et al., 1990). Mantle density thus vary from 3.3 g/cm^3 for fresh peridotites up to 2.55 g/cm^3 for totally serpentinized ones as evidenced by numerous studies on samples from Oman, Greece and Alps outcropping mantle body as well as mid Atlantic ridges (Bonnemains

et al., 2016); Indian ridge (Chen et al., 2021); and Tibet ophiolites (Li et al., 2017). Mantle density rock values listed in Table S1 in Supporting Information S1 and used for regional 2D forward modeling show a wide range of density varying from 3.3 to 2.90 g/cm^3 (García-Senz et al., 2020; Grandjean, 1994; Martin et al., 2017; Pedreira et al., 2007; Pueyo et al., 2015; Torné et al., 1989; Vacher & Souriau, 2001; Wehr et al., 2018). The magnetic susceptibility of serpentinized peridotites increases with modal amounts of magnetite (Bina & Henry, 1990; Nazarova, 1994). Based on a large data set of variably serpentinized peridotites, Maffione et al. (2014) reported a wide range of magnetic susceptibility values, ranging from 0.0007 up to 0.0758 SI, with an average value of 0.014 SI. They show that values higher than 0.02 SI were observed only for samples with a degree of serpentinization higher than 55%–60%. Other studies shows that magnetic susceptibility of highly serpentinized mantle can exceptionally reach 0.12 to 0.15 SI (Bonnemains et al., 2016; Chen et al., 2021; Krammer, 1990). According to all the above-mentioned literature, we modelized mantle serpentinization hypotheses with a wide range of density (3.3–2.7 g/cm^3) and magnetic susceptibility (0–0.06 SI). We discuss the signification of these values in terms of serpentinization degree in the discussion section.

4. Joint Gravimetric and Magnetic Modeling Results

4.1. North-South Section

On the north-south section, both the gravimetric and magnetic signals display a high amplitude and long wavelength positive anomaly of respectively +24.17 mGal and +10.02 nT (Figures 3 and 4). Because of the wavelength and intensity of these anomalies, modeling shows that the source body must be deeper than 8 km. Two models were produced along the N-S cross-section. The first model 1A is characterized by a homogeneously serpentinized mantle, modeled with a density of 2.9 g/cm^3 and a magnetic susceptibility of 0.01 SI (Figure 3). Although the model 1A correctly matches the gravimetric signal, it fails to reproduce the magnetic one (Table 1). The second model 1B (Figure 4), reveals that the mantle needs to be gradually serpentinized with different serpentinization fronts characterized by decreasing density (from 3.3 to 2.7 g/cm^3) and increasing magnetic susceptibility (from 0 SI to 0.06 SI) to reproduce both the gravimetric and magnetic signals (Table 1). One major outcome arising from model 1B is that both the high amplitude and long wavelength magnetic and gravimetric positive anomalies can be explained by the presence of the mantle at a depth varying from 8 km to the south (near the Axial Zone) to 10 km to the north (near to the preserved European margin). Even if these two anomalies are aligned with the mantle at depth, the magnetic anomaly is slightly shifted from 4 km toward the south with respect to the gravimetric anomaly. Model 1B also shows that the only way to generate this offset is to tilt the serpentinization fronts from around 10° to 25° toward the north (Figure 4). The magnetic signal displays a second positive anomaly of 4.95 nT localized to the south of the section. Considering the short wavelength of this anomaly, the modeling result shows that its source needs to be relatively shallow. The latter seems to coincide with the presence of the exposed basement of the Axial Zone (Figures 3 and 4). Finally, model 1B reveals that the former Early Cretaceous European rifted margin has been slightly inverted and mostly preserve its pre-collisional configuration while the Iberian margin suffered significant continental crustal thickening due to collisional nappe-stacking.

4.2. West-East Section

Building upon the results of the north-south section, the serpentinization fronts have been incorporated into the three west-east models presented in the paper (models 2B, 3B, and 4B; respectively Figures 5–7). For the sake of clarity, each of the three west-east models presented here were produced without the serpentinization fronts and are available in Figure S2 (model 2A), Figure S3 (model 3A) and Figure S4 (model 4A) in Supporting Information S1. However, none of these models allow the gravimetric and magnetic signals to be correctly adjusted (Table 1). Considering the lobate shape of the gravimetric anomaly that is characterized by two maxima (+20.57 mGal to the west and +24.17 mGal to the central part of the section), the corresponding dense body must consist of two separate parts or two different bodies to coincide with the structure suggested by the gravimetric data. Considering the short wavelength of the western +20.57 mGal anomaly, the modeling result shows that its source needs to be relatively shallow. The latter clearly coincides with the outcropping weathered UrG (Figures 5–7). As for the north-south section, modeling results highlight that the +24.17 mGal high amplitude and long wavelength anomaly is clearly related to the presence of lithospheric mantle at a depth of 8–10 km. As in model 1B, the models 2B, 3B, and 4B reveal that the serpentinization gradually increases from bottom to top as shown by the upward decrease in density and increase in magnetic susceptibility (Figures 5–7). The models 2B,

10.1029/2024TC008385

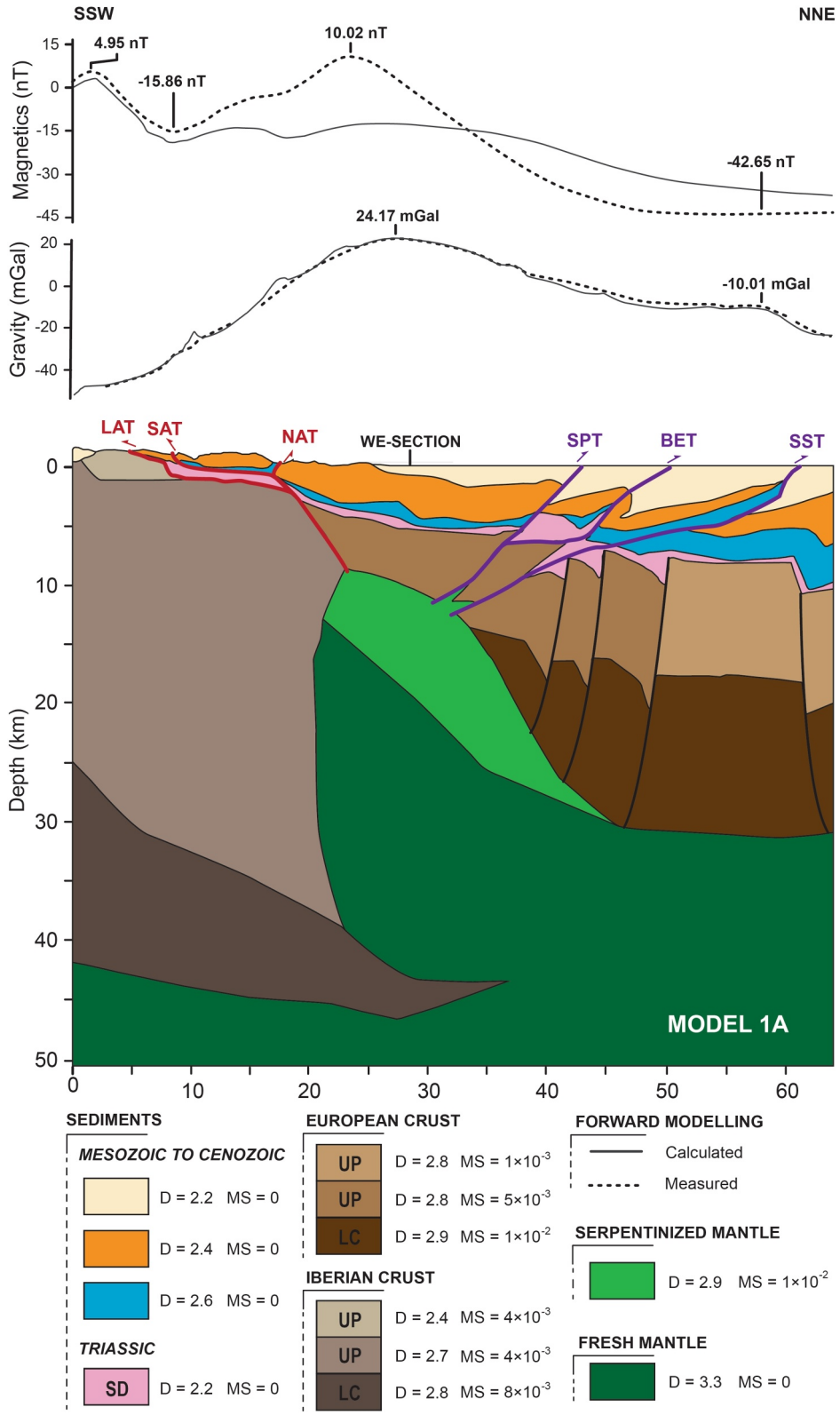

Figure 3. Geophysical forward modeling of the Mauléon basin along a SSW-NNE cross-section. Model 1A testing the hypothesis of uniformly serpentinized mantle. UP: Upper Crust; LC: Lower Crust; SD: Salt dominated Triassic. Modeling parameters: D: rock density, MS: magnetic susceptibility. Thrust faults: LAT: Lakhoura, SAT: South Arbailles, NAT: North Arbailles, SPT: Saint-Palais, BET: Bellevue, SST: Sainte-Suzanne. Location in Figure 2.

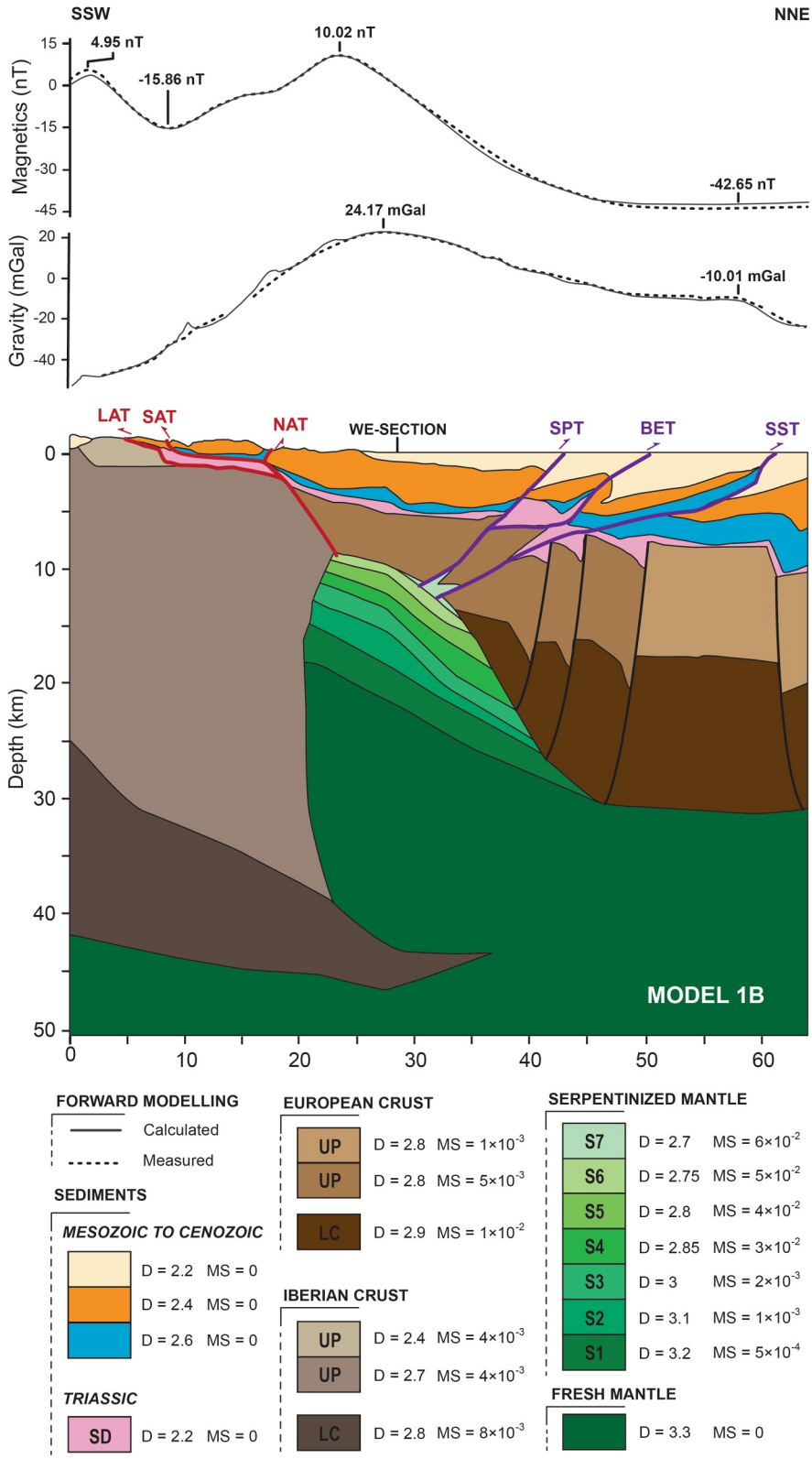

Figure 4. Geophysical forward modeling of the Mauléon basin along a SSW-NNE cross-section. Model 1B testing the hypothesis of a serpentinized mantle with a petrophysical gradient of serpentinization increasing from bottom to top. Modeling parameters: D rock density, MS magnetic susceptibility. S1–S7: Serpentinized fronts; UP: Upper Crust; LC: Lower Crust; SD: Salt dominated Triassic. Thrust faults: LAT Lakhoura, SAT: South Arbailles, NAT: North Arbailles, SPT: Saint-Palais, BET: Bellevue, SST: Sainte-Suzanne. Location in Figure 2.

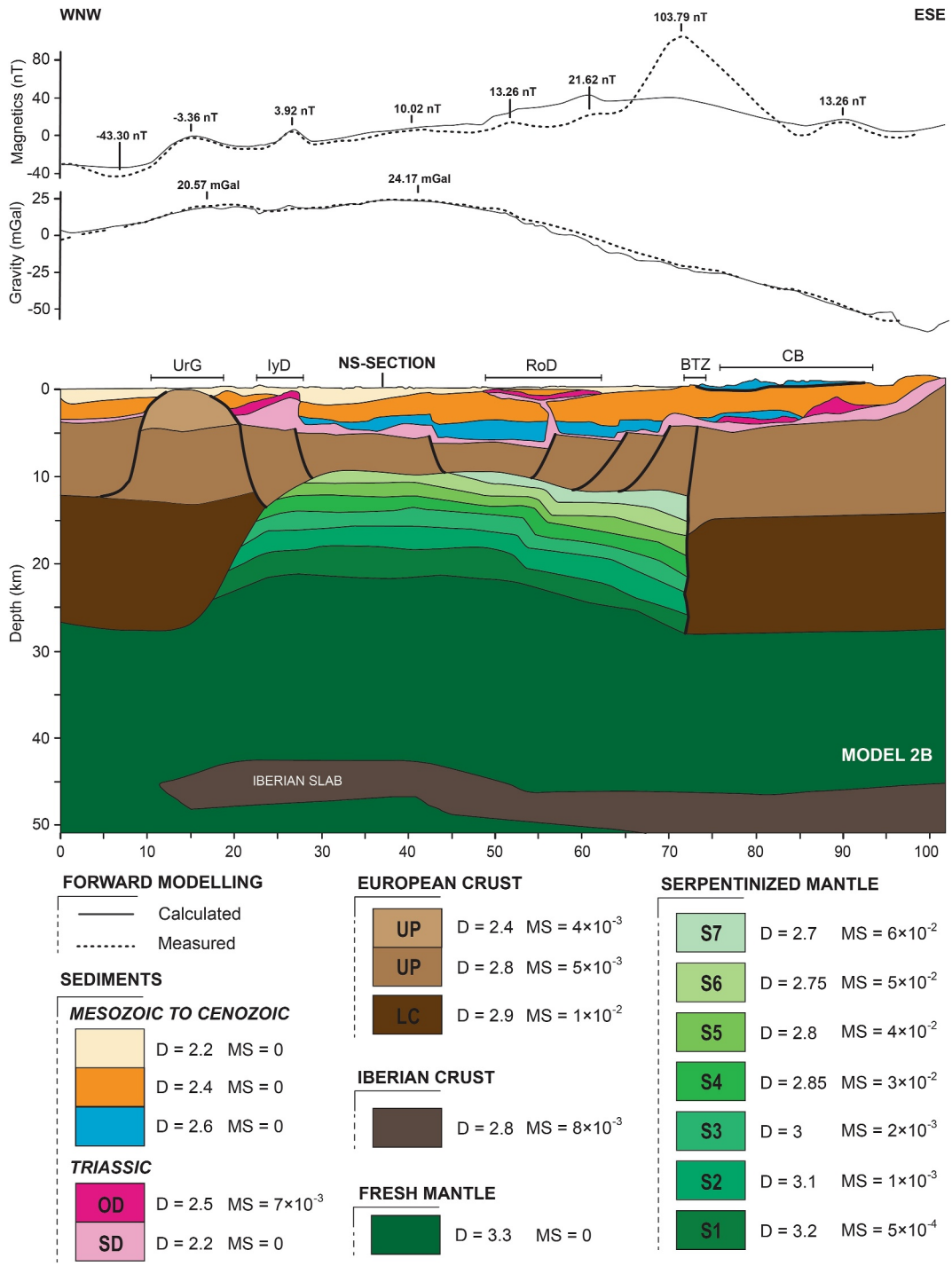

Figure 5. Geophysical forward modeling of the Mauléon basin along a WNW-ESE cross-section. Model 2B testing the hypothesis of a serpentinized mantle with a petrophysical gradient of serpentinization increasing from bottom to top. S1–S7: Serpentinized fronts; UP: Upper Crust; LC: Lower Crust; OD: Ophite dominated Triassic; SD: Salt dominated Triassic. Modeling parameters: D: rock density, MS: magnetic susceptibility. UrG: Ursuya granulites; IyD: Iholdy diapir; RoD: Roquiague diapir; BTZ: Barlanès transfer zone; CB: Chaînons Béarnais. Location in Figure 2.

3B, and 4B are consistent with the passive seismic acquisitions data (Lehujeur et al., 2021) showing that the sub-vertical BTZ delimits a western domain where mantle rocks are present at shallow depth from an eastern domain characterized by a thick continental crust. Although the lithological change is abrupt and the Barlanès structure is

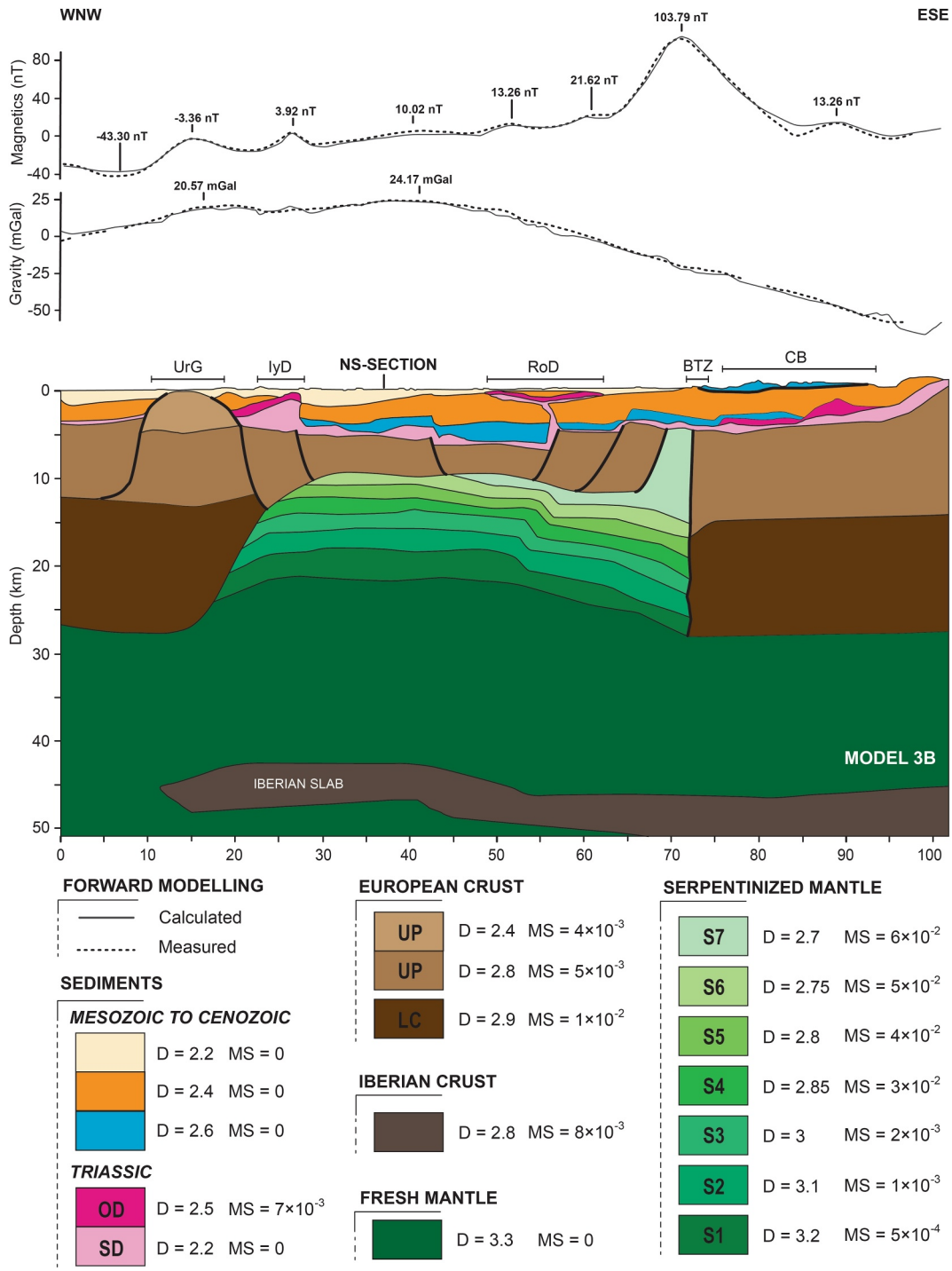

Figure 6. Geophysical forward modeling of the Mauléon basin along a WNW-ESE cross-section. Model 3B testing the hypothesis of a serpentinized mantle with a petrophysical gradient of serpentinization increasing from bottom to top and the presence of shallow mantle against the Barlanès transfer zone. S1–S7: Serpentinized fronts; UP: Upper Crust; LC: Lower Crust; OD: Ophite dominated Triassic; SD: Salt dominated Triassic. Modeling parameters: D: rock density, MS: magnetic susceptibility. UrG: Ursuya granulites; IyD: Iholdy diapir; RoD: Roquiague diapir; BTZ: Barlanès transfer zone; CB: Chaînons Béarnais. Location in Figure 2.

10.1029/2024TC008385

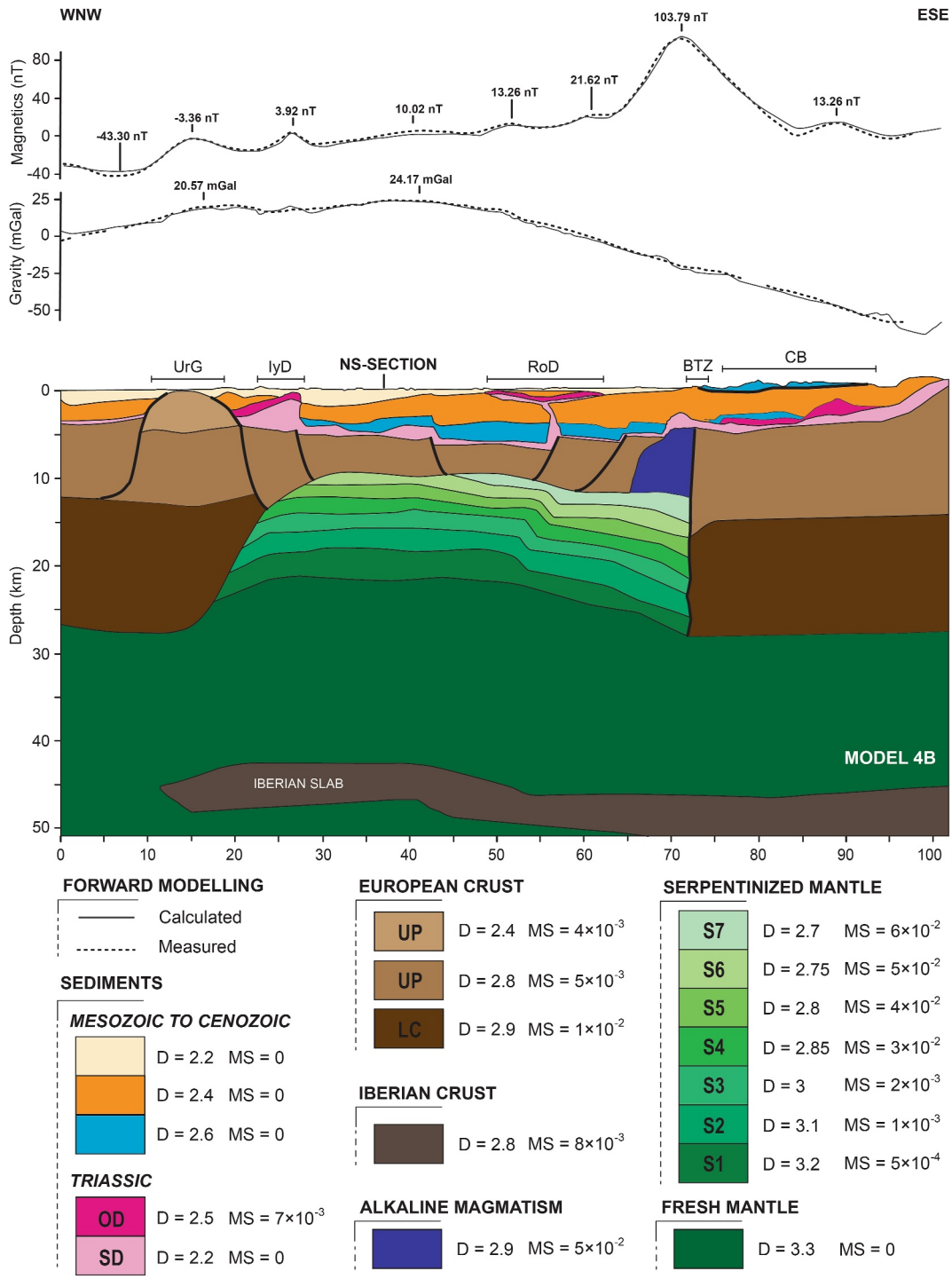

Figure 7. Geophysical forward modeling of the Mauléon basin along a WNW-ESE cross-section. Model 4B testing the hypothesis of a serpentinized mantle with a petrophysical gradient of serpentinization increasing from bottom to top and the presence of shallow alkaline magmatism against the Barlanès transfer zone. S1–S7: Serpentinized fronts; UP: Upper Crust; LC Lower Crust; OD: Ophite dominated Triassic; SD: Salt dominated Triassic. Modeling parameters: D rock density, MS magnetic susceptibility. UrG: Ursuya granulites; IyD: Iholdy diapir; RoD: Roquiague diapir; BTZ: Barlanès transfer zone; CB: Chaînons Béarnais. Location in Figure 2.

sub-vertical, the gravimetric signal gradually decreases crossing the BTZ. Thus, this significant change in upper lithospheric architecture from both side of the BTZ (mantle to the west vs. continental crust to the east) does not allow to explain the progressive decrease in gravimetric signal toward the east by itself. Geophysical modeling shows that to fit the progressive decrease in density toward the east, the serpentinization fronts need to be slightly inclined in this same direction (Figures 5–7). This geometry of the serpentinization fronts induces a gradual density transition crossing the BTZ from decreasing density in the uppermost serpentinized mantle (western Mauléon segment) to low density within the "Chainons Béarnais" continental crust (eastern Mauléon segment). Even if the model 2B reproduces very well the gravimetric signal (Figure 5), it fails to reproduce the magnetic one (Table 1). One major outcome arising from model 2B is that the mantle piece, localized at a depth of 8–10 km, do not allow to reproduce the main magnetic anomaly upon the BTZ (Figure 5). Indeed, this high amplitude anomaly reaching +103.79 nT appears to be shifted toward the east from the main +24.17 mGal gravimetric anomaly. This observation implies that their source is different. Other outcome arising from the failing model 2B is that the short wavelength of this high amplitude magnetic anomaly requires a shallow source located in between 4 and 10 km depth to properly fit the magnetic signal. Considering the strong intensity of the magnetic signal, modeling results also reveal that the magnetic body must either be very thick and/or have an extremely high magnetic susceptibility. Moreover, the absence of any gravimetric anomaly correlated with this magnetic anomaly attests that the magnetized body must have a density close to its surroundings (continental crust properties: density of 2.8 g/cm^3). Considering the geological context, two type of lithology could generate such anomaly into the basin, model 3B tested the presence of highly serpentinized mantle (density of 2.7 g/cm^3 and magnetic susceptibility of 0.06 SI; Figure 6) while model 4B tested the presence of alkaline magmatism (density of 2.9 g/cm^3 and magnetic susceptibility of 0.05 SI; Figure 7). Models 3B and 4B both successfully reproduce the gravimetric and magnetic signals and are both geologically consistent (Table 1). We discuss their implications in terms of basin evolution and hydrogen exploration potential in the discussion section.

Along the west-east transect five shorts wavelength and low amplitude magnetic signals are observed. As we move westwards, away from the magnetic mantle, the magnetic signal becomes negative. Despite being negative, a peak of −3.36 nT is observable in the most eastern part of the transect. This peak is correlated with the presence at the outcrop of the UrG, which also generate the short wavelength gravity anomaly located to the west of the transect (+20.57 mGal) (Figures 6 and 7). Moving toward the east, three pics are visible on the magnetic signal between the UrG and the BTZ: from west to east +3.92, +13.26, and +21.62 nT (Figures 6 and 7). Another peak is localized to the east of the Barlanès structure: +13.26 nT (Figures 6 and 7). Due to the very short wavelength of these magnetic anomalies, modeling shows that the source must be shallower than 4 km, so within the sedimentary cover. Models 3B and 4B reveal that these anomalies are linked to the very well-known early Cretaceous diapirs developed above preserved syn-rift normal faults (Figures 6 and 7). These diapirs have been both recognized at the outcrop scale and in seismic reflexion profiles as the Iholdy, Roquiague and CB diapiric systems (Canérot, 1988, 1989; Canérot et al., 2005; Labaume & Teixell, 2020; Saspiturry et al., 2022). As for the north-south profile (model 1B; Figure 4), the models 3B (Figure 6), and 4b (Figure 7) reveal that the mantle is responsible for a long wavelength and low amplitude magnetic anomaly of around +10.02 nT. This anomaly is less visible in the west-east profile due to the low wavelength and high amplitudes magnetic anomalies which slightly mask this signal.

5. Discussion

5.1. Distribution of Serpentinization and Alkaline Magmatism

Joint gravimetric and magnetic forward modeling reveals the occurrence of serpentinized mantle being at the origin of the long-wavelength gravimetric (+24.17 mGal) and magnetic (+10.02 nT) anomalies recognized in the basin. The north-south model 1B (Figure 4) highlights that the serpentinization is more pronounced toward the north as shown by: (a) the presence of the uppermost front characterized by a density of 2.7 g/cm^3 and a magnetic susceptibility of 0.06 SI only at the foot of the inverted European margin and (b) the fact that the serpentinization fronts are inclined toward the north of around 10°–25°. This orientation matches that of detachment systems recognized within the former Mauléon basin hyperextended domain, which exhumed the mantle rock and exposed it to serpentinization during the Early Cretaceous rifting (Jammes et al., 2009; Masini et al., 2014;

Saspiturry, Razin, et al., 2019; Saspiturry, Allanic, et al., 2020). The geometry of these northward dipping detachments is consistent with the northward increase in serpentinization inferred from our north-south geophysical model 1B (Figure 4).

The west-east model 2B highlights that serpentinization gradually increases toward the east reaching its maximum value in the vicinity of the BTZ (Figure 5). This observation is supported by the facts that the: (a) uppermost serpentinization front is only localized in the easternmost part of the mantle body and (b) serpentinization fronts are all inclined toward the east toward the BTZ. The eastward increase of serpentinization revealed by 2D geophysical forward modeling is consistent with paleogeographic reconstructions (Saspiturry, Issautier, Razin, Andrieu, et al., 2021) and restored cross-sections (Lescoutre and Manatschal., 2020; Saspiturry, Allanic, et al., 2020; Teixell et al., 2016) demonstrating that denudation of mantle rock was only achieved in the easternmost part of the Mauléon basin. Indeed, clasts of subcontinental mantle rocks have been reworked into the uppermost Albian to lower Cenomanian Urdach breccias only in the vicinity of the Barlanès structure (Debroas et al., 2010; Duée et al., 1984; Fortané et al., 1986; Roux, 1983). This inferred increase in serpentinization amount both toward the north and the east may be correlated with the Late Jurassic to Cenomanian change in kinematics of the Iberia and Eurasia plates from NE-SW orthogonal rifting to more transtensional WNW-ESE rift opening (Asti et al., 2022) generating respectively the northward and eastward serpentinization gradient recognized into the Mauléon basin. Thus, these observations suggest that at least part of the serpentinization is related to the Early Cretaceous hyperextension since the two recognized serpentinization gradients fit the palinspastic reconstructions of the syn-rift basin (Canérot, 2017; Canérot & Mediavilla, 2023; Saspiturry, Issautier, Razin, Andrieu, et al., 2021).

Models 3B (Figure 6) and 4B (Figure 7) show that two geological hypotheses allow to reproduce the short wavelength and high amplitude Barlanès magnetic anomaly (+103.79 nT): highly serpentinized mantle versus alkaline magmatism both localized at shallow depth and being shifted from the main serpentinized mantle body. The hypothesis of a mantle piece pinched along the BTZ is consistent with the lithospheric nature of this structure. Indeed, it localized mantle exhumation during the paroxysm of the Cretaceous rifting stage (Debroas et al., 2010; Saspiturry, Issautier, Razin, Andrieu, et al., 2021) and then segmented the orogenic prism during the Pyrenean compression (Lehujeur et al., 2021; Saspiturry et al., 2022). Based on syn-rift paleogeography, some authors have already proposed that the Barlanès structure could materialized a tilted block of mantle during the final stage of Early Cenomanian crustal break-up (Debroas et al., 2010; Saspiturry, Issautier, Razin, Andrieu, et al., 2021). The hypothesis defended in model 4B is also consistent since the North Pyrenean Zone underwent widespread Mesozoic magmatic activity, attested by Cretaceous alkaline magmatism (Montigny et al., 1986; Rossy et al., 1992). The Cretaceous igneous rocks consist of alkaline basalt and trachyte, as well as intrusive teschenyte and syenite (Azambre & Rossy, 1976; Azambre et al., 1992; Thiébaut et al., 1979). The Cretaceous volcanism was predominantly submarine, characterized by pillow basalt and pyroclastic rocks. The position of these rocks within the Cretaceous sedimentary deposits ensures reliable biostratigraphic ages for this magmatic event, being late Albian (synrift) to Santonian (postrift) in the western Pyrenees (Casteras et al., 1970; Castañares et al., 1997; Lamolda et al., 1983; López-Horgue et al., 1999; Rat, 1959; Rat et al., 1983; Schoeffler et al., 1964). This magmatism is very well-known at the outcrop scale in the eastern part of the Mauléon basin as sills localized within the Cretaceous turbidites in the footwall of the Barlanès structure (Casteras et al., 1970). If the Barlanès magnetic anomaly is effectively related to a Cretaceous magmatic body, the latter would be the largest ever identified within the north-Pyrenean rift system. Such alkaline magmatic bodies have been modeled in the ocean-continent transition of passive margin such as the SW Iberian margin (Neres et al., 2018) and the Gulf of Lion margin (Canva et al., 2019) in a similar palinspatic position, that is, in between the domains of hyper-extended continental crust and exhumed sub-continental mantle. The alkaline magmatic body of model 4B is characterized by a dimension of around 8×8 km and generates a magnetic anomaly of +103.79 nT (Figure 7). It shares close similarities with the Portimão bank in terms of size (dimension of 10×5 km) and amplitude of inferred magnetic signal (+160 nT) (Neres et al., 2018). So, model 3B implies the presence of a tilted block of mantle localized along the Barlanès structure at the end of the rifting stage (Figure 8 top) while model 4B suggests that the Barlanès structure localized the premises of the lithospheric break-up aborted before oceanic spreading (Figure 8 bottom). However, even if this supposed magmatic body has a strong chance of being Cretaceous in age considering the paleogeography of the Albian-Cenomanian rifting, we cannot exclude that it could be late Variscan in age as the Pyrenees are also affected by a major phase of alkaline magmatism during Permian time (Bixel & Lucas, 1983; Gretter et al., 2015; Lago et al., 2004; Lloret et al., 2018; Lucas, 1985; Rodriguez-Mendez et al., 2014).

10.1029/2024TC008385

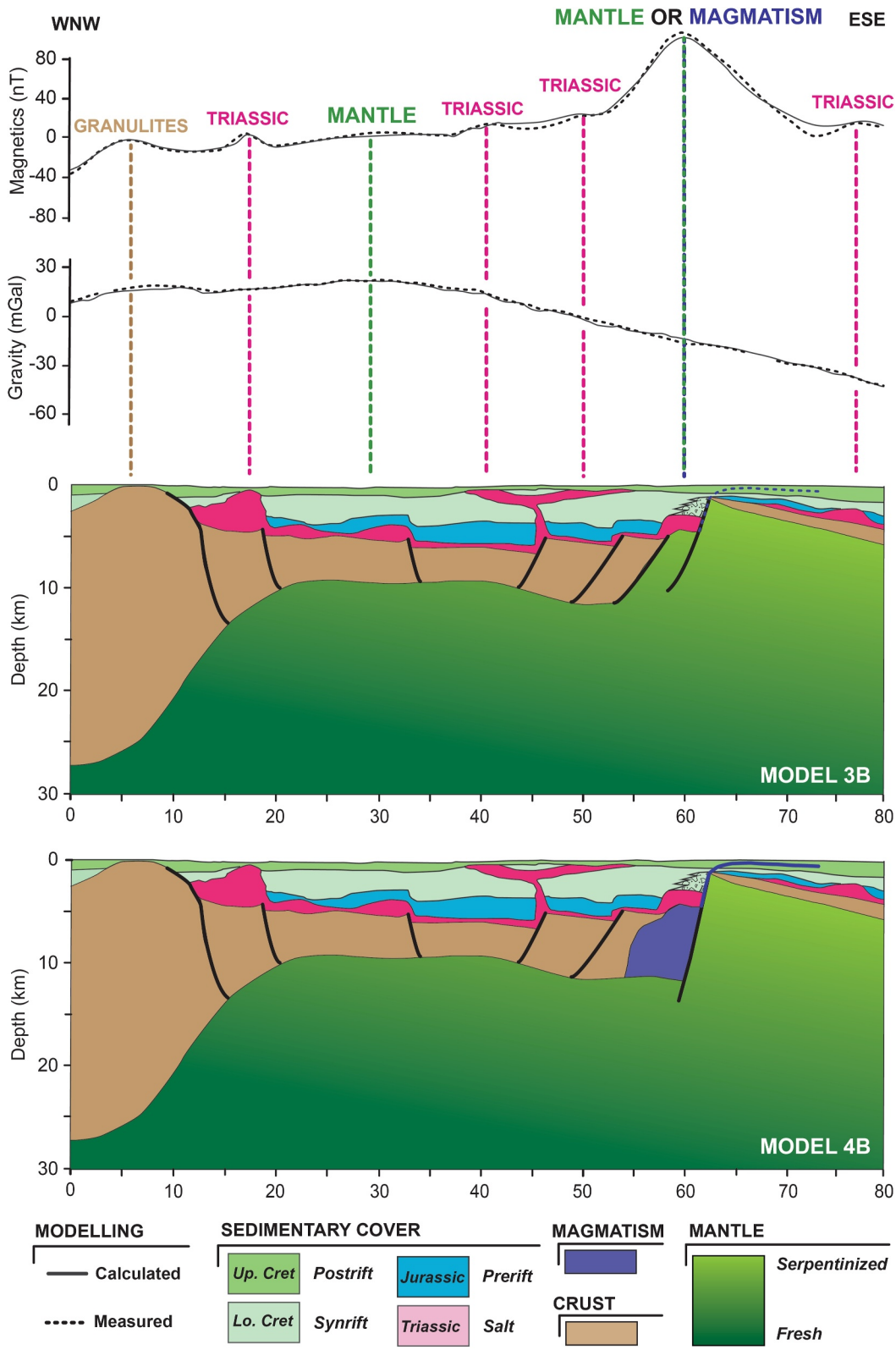

Figure 8. Schematic restoration of the WNW-ESE cross-section through the Mauléon basin hyperextended domain during the upper Cretaceous postrift stage. On top: current magnetic and gravimetric signal; On the middle: schematic restoration according to geophysical model 3B; On the bottom: schematic restoration according to geophysical model 4B.

10.1029/2024TC008385

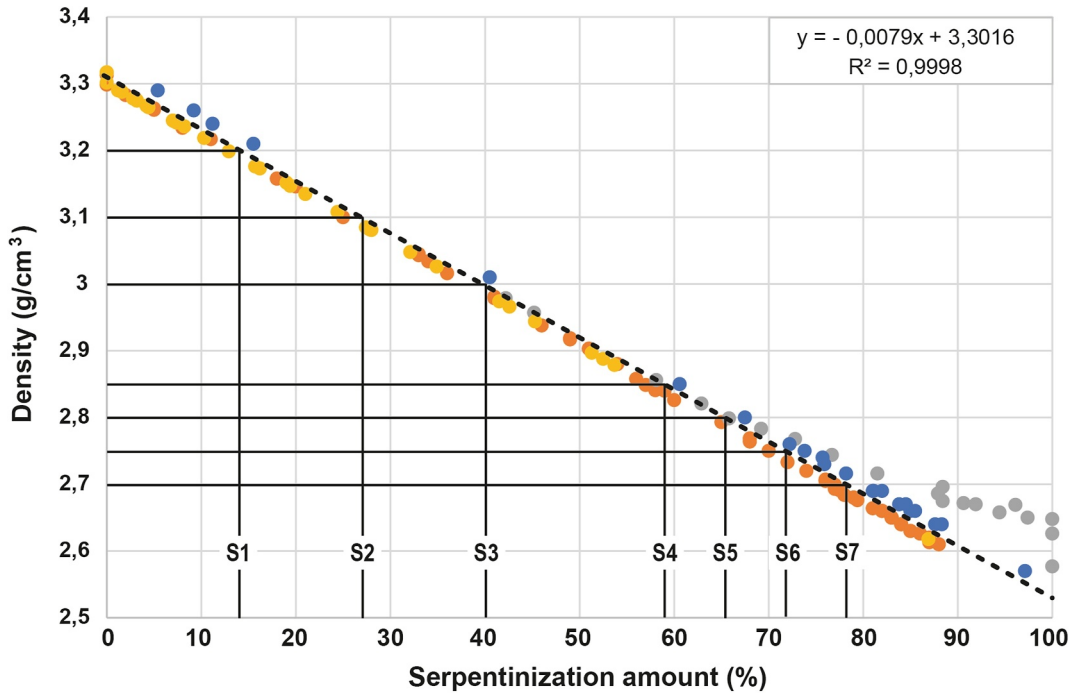

Figure 9. Graph showing the rate of serpentinization as a function of rock density. Data reported in this graph are from Chibati et al. (2022) (n = 22; blue data's), Li et al. (2017) (n = 34; yellow data's), Chen et al. (2021) (n = 20; gray data's) and Bonnemains et al. (2016) (n = 61; orange data's). The density of the serpentinization fronts S1–S7 from models 1B, 3B, and 4b have been reported on the graph to evaluate their amount of serpentinization.

5.2. Quantification of Serpentinization Degree

Geological models 1B and 2B show that the mantle is gradually serpentinized with seven different serpentinization fronts characterized by decreasing density (from 3.3 to 2.7 g/cm^3) and increasing magnetic susceptibility (from 0 SI to 0.06 SI) from 25 km depth to 10 km depth. It is very well established that increasing serpentinization degree is linearly correlated with decreasing mantle rock density from 3.35 g/cm^3 for fresh peridotites up to 2.45 g/cm^3 for totally serpentinized (Bina & Henry, 1990; Christensen, 1978; Krammer, 1990; Miller & Christensen, 1997; Nazarova, 1994; Oufi et al., 2002; Toft et al., 1990). It is therefore possible to use the modeled densities as an effective proxy for determining the average percentage of serpentinization within the modeled mantle fronts. The graph in Figure 9 shows mantle density as a function of serpentinization percentage and includes four recent studies with data from the Pyrenees (22 samples; Chibati et al., 2022), the Tibet (34 samples; Li et al., 2017), the Indian ridge (20 samples; Chen et al., 2021), the Oman, the Alps and the Atlantic Ocean (61 samples; Bonnemains et al., 2016). The linear regression line derived from these data (density = (−0.0079 × Serpentinization amount) + 3.3016) is similar to those proposed by Miller and Christensen (1999) and Oufi et al. (2002). By plotting in Figure 9, the density values used in the modeled serpentinization fronts, we estimate an average percentage value for the serpentinization rate for each front. Thus the mantle unit modeled under the Mauléon basin is gradually serpentinized on an overall thickness of around 15 km from 13% at the bottom up to 76% on top as follow: (Front 1) density of 3.2 g/cm^3 = ∼13%; (Front 2) density of 3.1 g/cm^3 = ∼26%; (Front 3) density of 3 g/cm^3 = ∼38%; (Front 4) density of 2.85 g/cm^3 = ∼57%; (Front 5) density of 2.8 g/cm^3 = ∼63%; (Front 6) density of 2.75 g/cm^3 = ∼70%; (Front 7) density of 2.7 g/cm^3 = ∼76% (Figure 9). Thus, the preserved Mauléon mantle unit share close similarities with the Gorringe Bank, in the distal domain of the SW Iberian margin, itself gradually serpentinized from 10% to 70% on a thickness of around 12 km (Sallarès et al., 2013). Despite the very high amplitude of its gravity anomaly, one of the largest on Earth, the Gorringe bank shows no significant magnetic anomaly, except for some short wavelength peaks likely due to local magmatic intrusions. The magnetic susceptibility of serpentinized peridotites increases with modal amounts of magnetite but without a clear linear relationship as for the density (Bina & Henry, 1990; Nazarova, 1994). Based on a large data set of variably serpentinized peridotites, Maffione et al. (2014) show that magnetic susceptibility values higher than 0.02 SI were observed only for samples with a

degree of serpentinization higher than 55%–60%. Our geophysical models 1B, 3B, and 4B appear consistent with these results since magnetic susceptibilities of more than 0.03 SI are only reported for fronts 4 to 7, characterized by a serpentinization degree higher than 57% according to their density.

Our results agree with recent studies of serpentinization quantification degree performed on the north-Pyrenean outcropping peridotites. Indeed, based on 22 samples along the whole north-Pyrenean zone, Chibati et al. (2022) have highlighted that mantle rocks are characterized by rock density of 3.29 g/cm^3 for fresh peridotites up to 2.5 g/cm^3 for totally serpentinized ones. Loiseau et al. (2024) have shown that the Turon de la Técouère mantle outcrop, in the eastern part of the Mauléon basin, is heterogeneously serpentinized from 3% up to 62%. For this same range of serpentinization degree, they measured magnetic susceptibility from 10–6 SI to 10–2 SI in terms of order of magnitude and rock density of 2.81–3.28 g/cm^3. Published works on the north-Pyrenean mantle bodies all agree on the fact that the mantle is serpentinized in a very heterogeneous way at the outcrop scale, ranging from an almost fresh mantle to a completely serpentinized one (Chibati et al., 2022; de Saint-Blanquat et al., 2016; Loiseau et al., 2024; Tichadou et al., 2021). Thus, given the variability of serpentinization amount at the outcrop scale, the percentage of serpentinization deduced from our study for each front must be considered as an average value. The significant amount of serpentinization reached in the uppermost part of the mantle (76% in the serpentinization front 7) could have been favored by preferential fluid-circulation within the main exhuming tectonic contact during early Cretaceous rifting. Indeed, the preserved north-Pyrenean zone detachments are known to favor the development of intense serpentinization on top of the mantle during continental crust hyperextension, as described in the Urdach and Saraillé massifs in the eastern Mauléon basin (Asti et al., 2019; Lagabrielle, Asti, Fourcade, Corre, Poujol, et al., 2019; Lagabrielle, Asti, Fourcade, Corre, Uzel, 2019), the Moncaup (Lagabrielle et al., 2010), and the Bestiac peridotite(s) in the central Pyrenees (de Saint Blanquat et al., 2016).

V_p seismic velocities of peridotites with a serpentinization degree higher than 75% can reach 4.5–5.5 km/s (Canales et al., 2000; Carlson & Miller, 2003; Christensen, 1978; Horen et al., 1996; Miller & Christensen, 1997; Sallarès et al., 2013). So, it is challenging to differentiate crustal and upper mantle rocks using only *P*-wave seismic velocities because serpentinized upper mantle can show a wide-range of velocities (~4.5–8.5 km/s), depending on the degree of serpentinization (Boddupalli et al., 2022; Chian et al., 1995; Christensen, 2004; Keen et al., 2018; Sallarès et al., 2013). Carlson and Miller. (2003) demonstrated that V_p velocities are linearly correlated with the serpentinization amount. In models 3B and 4B, the mantle is serpentinized at 13% (Front 1) at 20 km depth and 63% (Front 5) at 10 km depth in the western Mauléon mantle piece. Consequently, the corresponding expected velocities should decrease from 7.8 km/s at 20 km depth to 6.0 km/s at 10 km depth. On the same way, in the eastern part of the west-east section, the mantle is serpentinized at 38% (Front 3) at 20 km depth and reaches 76% (Front 7) in between 12 and 5 km depth depending on the models with corresponding expected V_p seismic values of respectively ~6.8 km/s at the bottom and ~5.4 km/s on top of the mantle. Passive seismic acquisitions present consistent V_p values with the expected ones deduced from the serpentinization amount evaluation (Figure S1C in Supporting Information S1; Lehujeur et al., 2021; Saspiturry et al., 2022). Indeed, they show decreasing V_p seismic velocities from ~8 km/s at 20 km depth up to ~6.5 km/s at 10 km depth in the western part of the mantle body while V_p velocities decrease from ~7 km/s at 20 km depth up to ~5.5 km/s at 5 km depth in its eastern part.

5.3. Implication for H2 Exploration

Joint forward geophysical modeling reveals that the high amplitude and long wavelength gravimetric and magnetic anomalies are due to the presence of gradually serpentinized mantle over 15 km thick. To consider future H2 exploration, one major question must be addressed: is the mantle currently in optimal thermal conditions to generate H2? Indeed, recent studies reveal that H2 production derived from mantle serpentinization mainly depends on temperature conditions. Serpentinization reactions are fast at temperatures higher than 315°C, but H2 concentrations may be limited by the attainment of stable thermodynamic equilibrium between olivine and aqueous fluid (McCollom & Bach, 2009). Conversely, below 150°C, H2 generation is severely limited by slow reaction kinetics and partitioning of Fe(II) into brucite (McCollom & Bach, 2009). Consequently, rates of H2 generation increase steeply from 200 to 300°C, but drop off at lower and higher temperatures (McCollom et al., 2016). To investigate if the mantle is within the optimum thermal conditions, we positioned the current isotherms on both modeled sections (Figure 10) considering the 25.0 ± 2.7°C/km geothermal gradient estimated by Saspiturry, Lahfid, et al. (2020). Thus, following the linear regression derived from these data (T°C = (0.0252 × Depth) + 7.1291; Saspiturry, Lahfid, et al., 2020; Figure S1 in

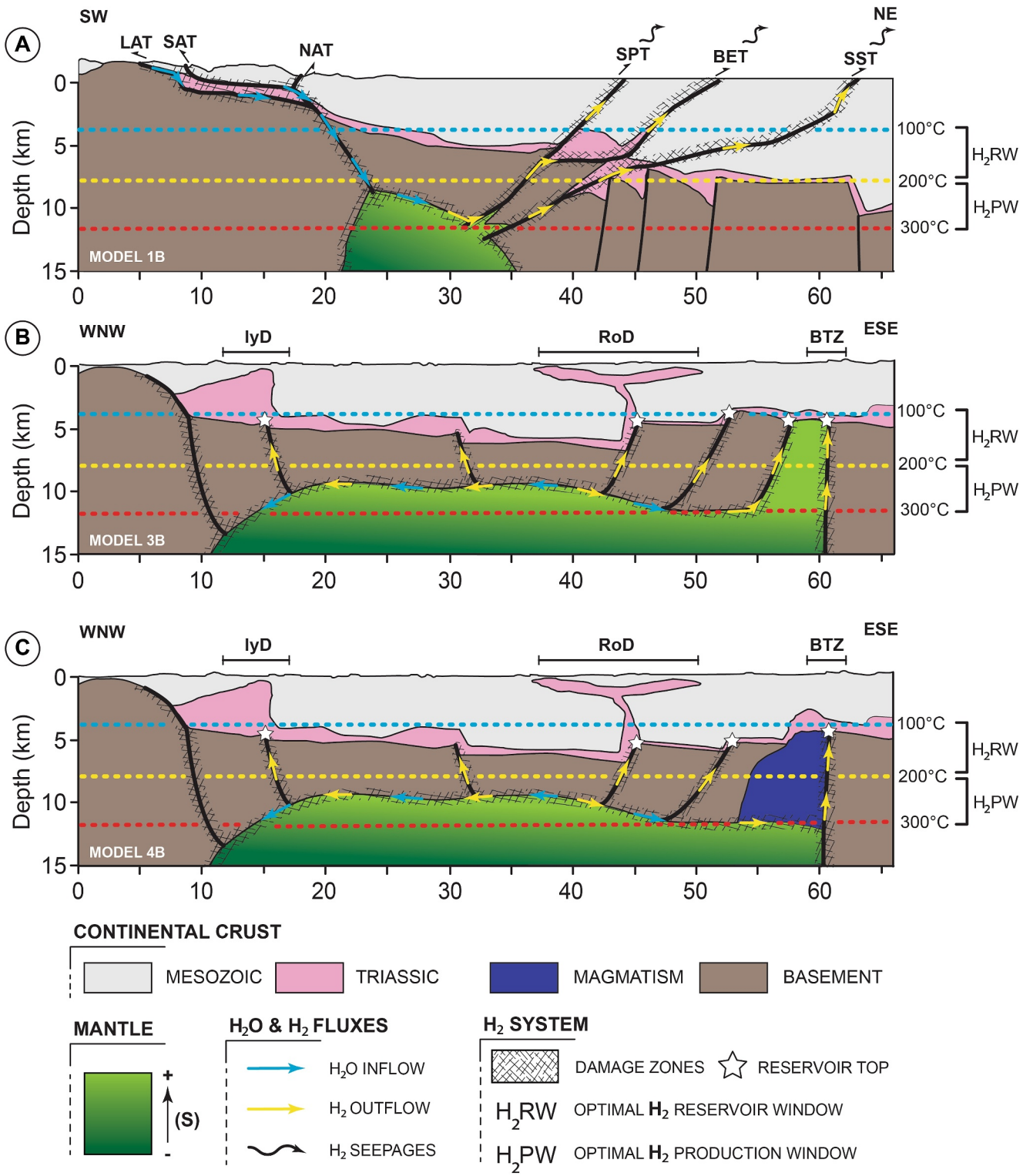

Figure 10. Conceptual model of the Mauléon basin H2 life cycle. (a) SSW-NNE cross-section from geophysical model 1B; (b) WNW-ESE cross-section from geophysical model 3B and (c) WNW-ESE cross-section from geophysical model 4B showing H2 production window (H2PW), H2 reservoir window (H2RW) and potential hydrogen plays. (S): serpentinization amount. Modeling parameters: D rock density, MS magnetic susceptibility. Thrust faults: LAT Lakhoura, SAT South Arbailles, NAT North Arbailles, SPT Saint-Palais, BET Bellevue, SST Sainte-Suzanne. Transfer zones: ITZ Iholdy, STZ Saison, BTZ Barlanès. BTZ: Barlanès transfer zone; IyD: Iholdy diapir; RoD: Roquiague diapir.

Supporting Information S1): the 100, 200, and 300°C isotherms are expected to be encountered at ~3,700, ~7,700, and ~11,600 m depth. The 200 and 300°C isotherms representing the optimum H2 production window (H2PW) are thus restricted to depths between 7.7 and 11.6 km (Figure 10). According to models 1B (Figures 10a), 3B (Figures 10b), and 4B (Figure 10c), a mantle thickness of 2.5–4 km is currently included in the H2PW. Estimated H2PW serpentinization amount (Section 5.2) is between 38% (Front 4) and 76% (Front 7) on the north-south section while is ranging between 63% and 76% on the west-east section. Even if these estimations could appear relatively high, there is still a significant amount of H2 to be produced since the mantle is not fully serpentinized. Water is required to perform the serpentinization reactions. Thus, it remains to be seen whether the water supply is effective to H2PW depths. This issue has recently been discussed. Indeed, based on electrical resistivity data published by Campanyà et al. (2012), Lefeuvre et al. (2021) suggested that the very low electrical resistivity at a depth of 13 km could be related to the presence of fluids infiltrating along the Lakora thrust fault until the contact between the Axial Zone and the mantle. This interpretation implies that serpentinization could currently be active as suggested as well by the seismicity. Lehujeur et al. (2021) have shown a distributed seismicity within the mantel piece. The latter could be linked to active serpentinization. Indeed, the increase in volume that occurs during serpentinization can build up stress and trigger cracking that would promote seismicity within the mantle (Malvoisin et al., 2017). Thus, the seepages recorded at the surface today have a great chance of being the consequence of very recent production (Lefeuvre et al., 2022).

When considering H2 exploitation, plays need to be properly identified. Numerous works shed light on the fact that temperature has a significant impact on the reactivity of H2 at depth. The optimal H2 reservoir window (H2RW) is between 100 and 200°C as H2 is inert within this temperature range due to the kinetic inhibition of both biological and abiotic reactions. Indeed, at temperatures lower than 100°C, H2 is consumed by microbial activity while above 200°C, it can react with sulfate and carbonate (Lefeuvre et al., 2022; McCollom & Shock, 1997; Schwartz & Friedrich, 2006; Truche et al., 2009, 2010, 2020). Considering the current thermal gradient, the 100 and 200°C isotherms representing the H2RW are restricted to depths between 3.7 and 7.7 km (Figure 10). Some plays have already been proposed in a north-south section parallel to model 1B at around 20 km westward. These plays are localized at a depth of 2.8–4 km within the anticlines made up of folded Mesozoic to Triassic formations related to the NPFT system (Lefeuvre et al., 2022). Our WNW-ESE models 3B (Figure 6) and 4b (Figure 7) offer an original point of view along strike of the basin featuring new potential H2 plays. Both models reveals that the Barlanès structure is lithospheric and deeply rooted within the subcontinental mantle. The main difference between these two models lies in the nature of the lithology of the body against the uppermost part of the structure. Given the size and importance of the BTZ, there is a strong chance that it can act as an effective pathway to carry H2 upwards toward the basement/cover interface at ~4 km depth and ~110°C. Such a temperature is ideal for long term H2 trapping. The top of the Barlanès structure thus materialized a potential optimal play for trapping H2. However, this structure is localized in the vicinity of the largest recorded crustal instrumental event in the Pyrenees: the 1967 Arette earthquake (Ml 5.3–5.7, Souriau & Pauchet, 1998; Rigo et al., 2015; Sylvander et al., 2021). Thus, seismic hazard needs to be properly addressed for future exploration in the vicinity of this structure. Models 3B and 4B also reveal the presence of potential preserved normal faults affecting the basement. On Model 3B, the faulted basement top is localized at depth of 4 km (~95°C) to 4.5 km (~107°C) and is included in the uppermost part of the H2PW (Figure 10b). On Model 4B, the basement top is slightly deeper as it is between 4.5 km (~107°C) and 5.5 (~132°C) km depth (Figure 10c). These normal faults appear to be sealed by the upper Triassic sequence. Since no H2 seepages have yet been measured above these inherited N20° normal faults (Figure 2b) probably reflects that the Triassic salt-sequence represents a potential efficient caprock (Figures 10b and 10c). All these targets represent optimal plays because they (a) are connected to the 200–300°C H2PW, (b) are localized within the 100–200°C H2RW, and (c) offer potential permeable pathways through the fault damage zone beneath an effective Triassic caprock. However, many questions remain unanswered: (a) what is the extent of these structures? (b) do they have a high permeability? (c) what is the overall volume of mantle present in the H2PW and the proportion of mantle to be serpentinized and (d) how much hydrogen would still be produced if the mantle were entirely serpentinized? To assess this resource further, some of these questions could be addressed by creating a 3D geometrical model of the mantle present in the H2PW.

Following the Pyrenean belt toward the east, two other positive Bouguer anomalies (Lourdes and Saint-Gaudens) are localized within the North Pyrenean Zone and aligned parallel to the trend of the chain (Angrand

et al., 2018; Casas et al., 1997; Chevrot et al., 2018). Such as the Labourd gravity anomaly described in our paper, these anomalies are related to the presence at shallow depth of dense material (Casas et al., 1997; Grandjean, 1994; Muñoz, 1992; Roure et al., 1989). A growing scientific consensus proposes that the Saint-Gaudens anomaly, upon the Baronnies-Comminges cretaceous rift basin (Figure 1), is due to the presence of a shallow body of allochthonous mantle (~8–16 km depth) pushed northward onto the Aquitaine Basin on the NPFT system (Espurt et al., 2019). Thus, this area shares close similarities with the Mauléon Basin as a potential optimal fertile H2 system. It fulfills the following three conditions: potential (a) source zone for H2 generated by serpentinization at shallow depth, (b) mantle rocks within the H2PW considering a geothermal gradient of 25°C/km and (c) effective migration pathways rooted in the mantle source such as the NPFT as well as Triassic caprock. The Lourdes and Saint-Gaudens anomalies therefore represent key targets for replicating the joint gravimetric and magnetic modeling method applied in the Mauléon basin to gain a more precise understanding of the potential H2 source. Other adjacent sedimentary basins could be explored for their natural H2 potential. Indeed, the Late Jurassic to Early Cretaceous transtensional deformation at the Iberia-Eurasia diffuse plate boundary led to the development of several sedimentary basins (e.g., Asti et al., 2022) that have been mostly preserved from the Pyrenean compression, including the Parentis (Bois et al., 1997; Ferrer et al., 2008; Jammes et al., 2010), Basque-Cantabrian (García-Senz et al., 2020; Pedrera et al., 2017, 2020), Bay of Biscay (Thinon et al., 2003) and Columbrets (Etheve et al., 2018; Roma et al., 2018) syn-rift basins (Figure 1). They all share similar characteristics with the Mauléon basin: (a) the presence of a significant gravimetric anomaly aligned with the rift axis, (b) efficient caprock of Late Triassic to earliest Jurassic evaporites, (c) potential H2 source zones of serpentinized mantle at shallow depth, and (d) tectonic structures rooted in the mantle offering potential H2 pathways.

6. Conclusion

In this work we show that the mantle beneath the Mauléon basin is gradually serpentinized over a thickness of almost 15 km. Several kilometers of mantle are present in the H2PW. Although the H2PW mantle is serpentinized between 38% and 76%, there is still a significant amount of H2 to be produced if the entire mantle were to be serpentinized. The faulted basement/cover interface located within the H2RW represents a major target for trapping H2. Many questions remain to be answered, but there is no doubt that the basin has great potential for natural H2 exploration. This work demonstrates that joint gravimetric and magnetic forward modeling represents a proven efficient tool to study the overall architecture and amount of serpentinization of preserved mantle upon reactivated rift system. A similar approach should be used to explore the natural H2 potential of others sedimentary basins in the Pyrenean and analogous regions.

Data Availability Statement

The authors declare that the data supporting this study are available within the following data repository: Saspiturry et al. (2024), https://doi.org/10.17632/kmh5mr4dvp.1. The dataset includes the original gmsys files from Oasis Montaj software of 8 joint gravimetric and magnetic forward 2D modeling along two orthogonal geological transects through the upper lithospheric structures of the Mauléon basin. The dataset also contains the complete Bouguer anomaly, RTP anomaly and elevation grids used for the modeling.

Acknowledgments
This work is part of Saspiturry's postdoctoral research conducted under the supervision of Cécile Allanic as part of the OROGEN project, cofunded by Total S.A., BRGM, and CNRS. We thank OROGEN project managers Sylvain Calassou (Total), Emmanuel Masini (Total), Olivier Vidal (Centre National de Recherche Scientifique) and Isabelle Thinon (BRGM). We thank the French Geological Survey (BRGM) for supporting this work. We greatly thank the two reviewers and especially Marta Neres who allowed us to significantly improve this work thanks to her constructive comments. Finally, we would like to thank the editors Dr. Laurent Jolivet and Dr. Jacqueline Halpin.

References

Abrajano, T. A., Sturchio, N. C., Bohlke, J. K., Lyon, G. L., Poreda, R. J., & Stevens, C. M. (1988). Methane-hydrogen gas seeps, Zambales Ophiolite, Philippines: Deep or shallow origin? *Chemical Geology*, *71*(1), 211–222. https://doi.org/10.1016/0009-2541(88)90116-7

Abrajano, T. A., Sturchio, N. C., Kennedy, B. M., Lyon, G. L., Muehlenbachs, K., & Bohlke, J. K. (1990). Geochemistry of reduced gas related to serpentinization of the Zambales ophiolite, Philippines. *Applied Geochemistry*, *5*(5), 625–630. https://doi.org/10.1016/0883-2927(90)90060-I

Albarède, F., & Michard-Vitrac, A. (1978). Age and significance of the North Pyrenean metamorphism. *Earth and Planetary Science Letters*, *40*(3), 327–332. https://doi.org/10.1016/0012-821x(78)90157-7

Angrand, P., Ford, M., & Watts, A. B. (2018). Lateral variations in foreland flexure of a rifted continental margin: The Aquitaine Basin (SW France). *Tectonics*, *37*(2), 430–449. https://doi.org/10.1002/2017TC004670

Angrand, P., & Mouthereau, F. (2021). Evolution of the Alpine orogenic belts in the Western Mediterranean region as resolved by the kinematics of the Europe-Africa diffuse plate boundary. *BSGF Earth Sciences Bulletin*, *192*, 42. https://doi.org/10.1051/bsgf/2021031

Asti, R., Lagabrielle, Y., Fourcade, S., Corre, B., & Monié, P. (2019). How do continents Deform during mantle exhumation? Insights from the northern Iberia inverted Paleopassive margin, western Pyrenees (France). *Tectonics 2018TC005428*, *38*(5), 1666–1693. https://doi.org/10.1029/2018TC005428

Asti, R., Saspiturry, N., & Angrand, P. (2022). The Mesozoic Iberia-Eurasia diffuse plate boundary: A wide domain of distributed transtensional deformation progressively focusing along the North Pyrenean zone. *Earth-Science Reviews*, *230*, 104040. https://doi.org/10.1016/j.earscirev.2022.104040

Azambre, B., & Rossy, M. (1976). Le magmatisme alcalin d'âge crétacé, dans les Pyrénées occidentales et l'Arc basque; ses relations avec le métamorphisme et la tectonique. *Bulletin de la Societe Geologique de France*, *7*(6), 1725–1728. https://doi.org/10.2113/gssgfbull.S7-XVIII.6.1725

Azambre, B., Rossy, M., & Albarède, F. (1992). Petrology of the alkaline magmatism from the Cretaceous North-Pyrenean rift zone (France and Spain). *European Journal of Mineralogy*, *4*, 813–834. https://doi.org/10.1127/ejm/4/4/0813

Bina, M. M., & Henry, B. (1990). Magnetic properties, opaque mineralogy and magnetic anisotropies of serpentinized peridotites from ODP Hole 670A near the Mid-Atlantic Ridge. *Physics of the Earth and Planetary Interiors*, *65*(1–2), 88–103. https://doi.org/10.1016/0031-9201(90)90078-C

Bixel, F., & Lucas, C. L. (1983). Magmatisme, tectonique et sédimentation dans les fossés stéphano-permiens des Pyrénées occidentales. *Revue de Geologie Dynamique et de Geographie Physique*, *24*(4), 329–342.

Boddupalli, B., Minshull, T. A., Morgan, J., Bayrakci, G., & Klaeschen, D. (2022). Comparison of two- and three-dimensional full waveform inversion imaging using wide-angle seismic data from the Deep Galicia Margin. *Geophysical Journal International*, *227*(1), 228–256. https://doi.org/10.1093/gji/ggab164

Boillot, G., Recq, M., Winterer, E. L., Meyer, A. W., Applegate, J., Baltuck, M., et al. (1987). Tectonic denudation of the upper mantle along passive margins: A model based on drilling results (ODP leg 103, western Galicia margin, Spain). *Tectonophysics*, *132*(4), 335–342. https://doi.org/10.1016/0040-1951(87)90352-0

Bois, C., Gariel, O., Lefort, J.-P., Rolet, J., Brunet, M.-F., Masse, P., & Olivet, J. L. (1997). Geologic contribution of the bay of biscay deep seimic survey: A summary of the main scientific results, a discussion of the open questions and suggestions for further investigations. *Mémoires de La Société Géologique de France*, *171*, 193–209.

Bonnemains, D., Carlut, J., Escartín, J., Mével, C., Andreani, M., & Debret, B. (2016). Magnetic signatures of serpentinization at ophiolite complexes. *Geochemistry, Geophysics, Geosystems*, *17*(8), 2969–2986. https://doi.org/10.1002/2016GC006321

Campanyà, J., Ledo, J., Queralt, P., Marcuello, A., Liesa, M., & Muñoz, J. A. (2012). New geoelectrical characterisation of a continental collision zone in the West-Central Pyrenees: Constraints from long period and broadband magnetotellurics. *Earth and Planetary Science Letters*, *333*, 112–121. https://doi.org/10.1016/j.epsl.2012.04.018

Canales, J. P., Detrick, R. S., Lin, J., Collins, A., & Toomey, D. R. (2000). Crustal and upper mantle seismic structure beneath the rift mountains and across a non transform offset at the Mid-Atlantic Ridge (35N). *Journal of Geophysical Research*, *105*(B2), 2699–2719. https://doi.org/10.1029/1999JB900379

Canérot, J. (1988). Manifestations de l'halocinèse dans les chaînons béarnais (zone Nord-Pyrénéenne) au Crétacé inférieur. *Comptes rendus de l'Académie des sciences Série 2*, *306*(15), 1099–1102.

Canérot, J. (1989). Rifting éocrétacé et halocinèse sur la marge ibérique des Pyrénées Occidentales (France). *Bulletin Centres Recherches Exploration-Production Elf-Aquitaine*, *13*, 87–99.

Canérot, J. (2017). The pull apart-type Tardets-Mauléon Basin, a key to understand the formation of the Pyrenees. *Bulletin de la Societe Geologique de France*, *188*(6), 35. https://doi.org/10.1051/bsgf/2017198

Canérot, J., Hudec, M. R., & Rockenbauch, K. (2005). Mesozoic diapirism in the Pyrenean orogen: Salt tectonics on a transform plate boundary. *AAPG Bulletin*, *89*(2), 211–229. https://doi.org/10.1306/09170404007

Canérot, J., & Lenoble, J.-L. (1993). Diapirisme crétacé sur la marge ibérique des Pyrénées occidentales; exemple du pic de Lauriolle; comparaisons avec l'Aquitaine, les Pyrénées centrales et orientales. *Bulletin de la Societe Geologique de France*, *164*(5), 719–726.

Canérot, J., & Mediavilla, F. (2023). The Mid-Albian unconformity, a key to understand the geodynamics of the North Pyrenean Trough. *Bulletin de la Societe Geologique de France*, *194*(1), 4. https://doi.org/10.1051/bsgf/2023001

Cannat, M., Fontaine, F., & Escartín, J. (2010). Serpentinization and associated hydrogen and methane fluxes at slow spreading ridges. In P. A. Rona, C. W. Devey, J. Dyment, & B. J. Murton (Eds.), *Geophysical Monograph series* (Vol. 188, pp. 241–264). American Geophysical Union. https://doi.org/10.1029/2008GM000760

Canva, A., Thinon, I., Peyrefitte, A., Couëffé, R., Maillard, A., Jolivet, L., et al. (2019). The Catalan magnetic anomaly: Its significance for the crustal structure of the Gulf of Lion passive margin and relationship to the Catalan transfer zone. *Marine and Petroleum Geology*, *113*, 104174. https://doi.org/10.1016/j.marpetgeo.2019.104174

Carlson, R.-L., & Miller, D.-J. (2003). Mantle wedge water contents estimated from seismic velocities in partially serpentinized peridotites. *Geophysical Research Letters*, *30*(5), 1250. https://doi.org/10.1029/2002GL016600

Casas, A., Kearey, P., Rivero, L., & Adam, C. R. (1997). Gravity anomaly map of the Pyrenean region and a comparison of the deep geological structure of the western and eastern Pyrenees. *Earth and Planetary Science Letters*, *150*(1), 65–78. https://doi.org/10.1016/S0012-821X(97)00087-3

Castañares, L. M., Robles, S., & Vicente Bravo, J. C. (1997). Distribución estratigráfica de los episodios volcánicos submarinos del Albiense-Santoniense en la Cuenca Vasca (sector Gernika-Plentzia, Bizkaia). *Geogaceta*, *22*, 43–46.

Casteras, M., Villanova, M., Godechot, J., Blanc, C., Labourguigne, J., Deloffre, R., et al. (1970). Carte géologique de la France au 1/50 000: feuille de Lourdes, Orléans.

Chen, H., Tao, C., Revil, A., Zhu, Z., Zhou, J., Wu, T., & Deng, X. (2021). Induced polarization and magnetic responses of serpentinized ultramafic rocks from mid-ocean ridges. *Journal of Geophysical Research: Solid Earth*, *126*(12), e2021JB022915. https://doi.org/10.1029/2021JB022915

Chevrot, S., Sylvander, M., Diaz, J., Martin, R., Mouthereau, F., Manatschal, G., et al. (2018). The non-cylindrical crustal architecture of the Pyrenees. *Scientific Reports*, *8*(1), 9591. https://doi.org/10.1038/s41598-018-27889-x

Chian, D., Louden, K. E., & Reid, I. (1995). Crustal structure of the Labrador Sea conjugate margin and implications for the formation of nonvolcanic continental margins. *Journal of Geophysical Research*, *100*(B12), 24239–24253. https://doi.org/10.1029/95JB02162

Chibati, N., Géeraud, Y., & Essa, K. S. (2022). Petrophysical characterization and thermal conductivity prediction of serpentinized peridotites. *Geophysical Journal International*, *231*(3), 1786–1805. https://doi.org/10.1093/gji/ggac288

Christensen, N. I. (1978). Ophiolites, seismic velocities and oceanic crustal structure. *Tectonophysics*, *47*(1–2), 131–157. https://doi.org/10.1016/0040-1951(78)90155-5

Christensen, N. I. (2004). Serpentinites, peridotites, and seismology. *International Geology Review*, *46*(9), 795–816. https://doi.org/10.2747/0020-6814.46.9.795

Corre, B., Lagabrielle, Y., Labaume, P., Fourcade, S., Clerc, C., & Ballèvre, M. (2016). Deformation associated with mantle exhumation in a distal, hot passive margin environment: New constraints from the Saraillé Massif (Chaînons Béarnais, North-Pyrenean Zone). *Comptes Rendus Geoscience*, *348*(3–4), 279–289. https://doi.org/10.1016/j.crte.2015.11.007

Coveney, R. M., Jr., Goebel, E. D., Zeller, E. J., Dreschhoff, G. A. M., & Angino, E. E. (1987). Serpentinization and the origin of hydrogen gas in Kansas1. *AAPG Bulletin*, *71*(1), 39–48. https://doi.org/10.1306/94886D3F-1704-11D7-8645000102C1865D

Curnelle, R. (1983). Evolution structuro-sédimentaire du Trias et de l'Infra-Lias d'Aquitaine. *Bulletin Centre de Recherche Exploration Production Elf-Aquitaine*, *7*(1), 69–99.

Daignières, M., Séguret, M., Specht, M., & ECORS Team. (1994). *The Arzacq-western Pyrenees ECORS deep seismic profile* (pp. 199–208). Special Publication of the European Association of Petroleum Geoscientists.

Debroas, E. J., Canérot, J., & Bilotte, M. (2010). Les brèches d'Urdach, témoins de l'exhumation du manteau pyrénéen dans un escarpement de faille vraconnien-cénomanien inférieur (Zone nord-pyrénéenne, Pyrénées-Atlantiques, France). *Géologie de la France*, *2*, 53–63.

de Saint-Blanquat, M., Bajolet, F., Grand'Homme, A., Proietti, A., Zanti, M., Boutin, A., et al. (2016). Cretaceous mantle exhumation in the central Pyrenees: New constraints from the peridotites in eastern Ariege (North Pyrenean zone, France). *Comptes Rendus Geoscience*, *348*(3), 268–278. https://doi.org/10.1016/j.crte.2015.12.003

Deville, E., & Prinzhofer, A. (2016). The origin of N_2-H_2-CH_4-rich natural gas seepages in ophiolitic context: A major and noble gases study of fluid seepages in New Caledonia. *Chemical Geology*, *440*, 139–147. https://doi.org/10.1016/j.chemgeo.2016.06.011

Ducasse, L., & Vélasque, P.-C. (1988). Géotraverse dans la partie occidentale des Pyrénées, de l'avant-pays aquitain au bassin de l'Ebre: Effet d'une inversion structurale sur l'édification d'une chaîne intracontinentale. Université Paul Cézanne (Aix-Marseille). In *PhD, Faculté des sciences et techniques de Saint-Jérôme*.

Duée, G., Lagabrielle, Y., Coutelle, A., & Fortané, A. (1984). Les lherzolites associées aux chaînons béarnais (Pyrénées occidentales): Mise à l'affleurement anté-dogger et resédimentation albo-cénomanienne. *Comptes-rendus des séances de l'Académie des sciences. Série 2, Mécanique-physique, chimie, sciences de l'univers, sciences de la terre*, *299*(17), 1205–1210.

Espurt, N., Angrand, P., Teixell, A., Labaume, P., Ford, M., de Saint Blanquat, M., & Chevrot, S. (2019). Crustal-scale balanced cross-section and restorations of the Central Pyrenean belt (Nestes-Cinca transect): Highlighting the structural control of Variscan belt and Permian-Mesozoic rift systems on mountain building. *Tectonophysics*, *764*, 25–45. https://doi.org/10.1016/j.tecto.2019.04.026

Etheve, N., Mohn, G., Frizon de Lamotte, D., Roca, E., Tugend, J., & Gómez-Romeu, J. (2018). Extreme Mesozoic crustal thinning in the eastern Iberia margin: The example of the Columbrets basin (Valencia trough). *Tectonics*, *37*(2), 636–662. https://doi.org/10.1002/2017TC004613

Fabriès, J., Lorand, J.-P., & Bodinier, J.-L. (1998). Petrogenetic evolution of orogenic lherzolite massifs in the central and western Pyrenees. *Tectonophysics*, *292*(1), 145–167. https://doi.org/10.1016/S0040-1951(98)00055-9

Fabriès, J., Lorand, J.-P., Bodinier, J.-L., & Dupuy, C. (1991). Evolution of the upper mantle beneath the Pyrenees: Evidence from orogenic Spinel lherzolite massifs. *Journal of Petrology*, *2*, 55–76. https://doi.org/10.1093/petrology/Special_Volume.2.55

Ferrer, O., Roca, E., Benjumea, B., Muñoz, J. A., Ellouz, N., & MARCONI Team. (2008). The deep seismic reflection MARCONI-3 profile: Role of extensional Mesozoic structure during the Pyrenean contractional deformation at the eastern part of the Bay of Biscay. *Marine and Petroleum Geology*, *25*(8), 714–730. https://doi.org/10.1016/j.marpetgeo.2008.06.002

Fortané, A., Duée, G., Lagabrielle, Y., & Coutelle, A. (1986). Lherzolites and the western "Chaînons béarnais" (French Pyrenees): Structural and paleogeographical pattern. *Tectonophysics*, *129*(1), 81–98. https://doi.org/10.1016/0040-1951(86)90247-7

García-Senz, J., Pedrera, A., Ayala, C., Ruiz-Constán, A., Robador, A., & Rodríguez-Fernández, L. R. (2020). Inversion of the north Iberian hyperextended margin: The role of exhumed mantle indentation during continental collision. *Geological Society, London, Special Publications*, *490*(1), 177–198. https://doi.org/10.1144/SP490-2019-112

Gómez-Romeu, J., Masini, E., Tugend, J., Ducoux, M., & Kusznir, N. (2019). Role of rift structural inheritance in orogeny highlighted by the Western Pyrenees case-study. *Tectonophysics*, *766*, 131–150. https://doi.org/10.1016/j.tecto.2019.05.022

Grandjean, G. (1994). Etude des structures crustales dans une portion de chaîne et de leur relation avec les bassins sédimentaires. Application aux Pyrénées occidentales. *Bulletin des Centres de Recherches Exploration-Production Elf-Aquitaine*, *18*(2), 391–420.

Gretter, N., Ronchi, A., López-Gómez, J., Arche, A., De la Horra, R., Barrenechea, J., & Lago, M. (2015). The late Palaeozoic-early Mesozoic from the Catalan Pyrenees (Spain): 60 Myr of environmental evolution in the frame of the western peri-Tethyan palaeogeography. *Earth-Science Reviews*, *150*, 679–708. https://doi.org/10.1016/j.earscirev.2015.09.001

Horen, H., Zamora, M., & Dubuisson, G. (1996). Seismic waves velocities and anisotropy in serpentinized peridotites from Xigaze ophiolite: Abundance of serpentine in slow spreading ridge. *Geophysical Research Letters*, *23*(1), 9–12. https://doi.org/10.1029/95GL03594

Issautier, B., Saspiturry, N., & Serrano, O. (2020). Structural inheritance and salt tectonics controlling pseudosymmetric rift formation during Early Cretaceous hyperextension of the Arzacq and Tartas Basins (southwest France). *Marine and Petroleum Geology*, *118*, 104395. https://doi.org/10.1016/j.marpetgeo.2020.104395

James, V., & Canérot, J. (1999). Diapirisme et structuration post-triasique des Pyrénées occidentales et de l'Aquitaine méridionale (France). *Eclogae Geologicae Helvetiae*, *92*, 63–72.

Jammes, S., Manatschal, G., & Lavier, L. (2010). Interaction between prerift salt and detachment faulting in hyperextended rift systems: The example of the Parentis and Mauléon basins (Bay of Biscay and western Pyrenees). *AAPG Bulletin*, *94*(7), 957–975. https://doi.org/10.1306/12090909116

Jammes, S., Manatschal, G., Lavier, L., & Masini, E. (2009). Tectonosedimentary evolution related to extreme crustal thinning ahead of a propagating ocean: Example of the western Pyrenees. *Tectonics*, *28*(4), TC4012. https://doi.org/10.1029/2008TC002406

Keen, C. E., Dickie, K., & Dafoe, L. T. (2018). Structural characteristics of the ocean continent transition along the rifted continental margin, offshore central Labrador. *Marine and Petroleum Geology*, *89*, 443–463. https://doi.org/10.1016/j.marpetgeo.2017.10.012

Klein, F., Bach, W., Jöns, N., McCollom, T., Moskowitz, B., & Berquó, T. (2009). Iron partitioning and hydrogen generation during serpentinization of abyssal peridotites from 15°N on the Mid-Atlantic Ridge. *Geochimica et Cosmochimica Acta*, *73*(22), 6868–6893. https://doi.org/10.1016/j.gca.2009.08.021

Klein, F., Bach, W., & McCollom, T. M. (2013). Compositional controls on hydrogen generation during serpentinization of ultramafic rocks. *Lithos*, *178*, 55–69. https://doi.org/10.1016/j.lithos.2013.03.008

Krammer, K. (1990). Rock magnetic properties and opaque mineralogy of selected samples from Hole 670A. *Proceedings of the Ocean Drilling Program, Scientific Results*, *106/109*, 269–273.

Labaume, P., & Teixell, A. (2020). Evolution of salt structures of the Pyrenean rift (Chaînons Béarnais, France): From hyper-extension to tectonic inversion. *Tectonophysics*, *785*, 228451. https://doi.org/10.1016/j.tecto.2020.228451

Lagabrielle, Y., Asti, R., Duretz, T., Clerc, C., Fourcade, S., Teixell, A., et al. (2020). A review of cretaceous smooth-slopes extensional basins along the Iberia-Eurasia plate boundary: How pre-rift salt controls the modes of continental rifting and mantle exhumation. *Earth Science Review*, *201*, 103071. https://doi.org/10.1016/j.earscirev.2019.103071

Lagabrielle, Y., Asti, R., Fourcade, S., Corre, B., Poujol, M., Uzel, J., et al. (2019). Mantle exhumation at magma-poor passive continental margins. Part I. 3D architecture and metasomatic evolution of a fossil exhumed mantle domain (Urdach lherzolite, North-Western Pyrenees, France). *BSGF Earth Sciences Bulletin*, *190*, 8. https://doi.org/10.1051/bsgf/2019007

Lagabrielle, Y., Asti, R., Fourcade, S., Corre, B., Uzel, J., Labaume, P., et al. (2019). Mantle exhumation at magma-poor passive continental margins. Part II. Tectonic and metasomatic evolution of large displacement detachment faults preserved in a fossil distal margin domain (Saraillé lherzolites, north-western Pyrenees, France). *BSGF Earth Sciences Bulletin*, *190*(1), 14. https://doi.org/10.1051/bsgf/2019013

Lagabrielle, Y., Labaume, P., & de Saint Blanquat, M. (2010). Mantle exhumation, crustal denudation, and gravity tectonics during Cretaceous rifting in the Pyrenean realm (SW Europe): Insights from the geological setting of the lherzolite bodies. *Tectonics*, *29*(4), 190. https://doi.org/10.1029/2009TC002588

Lago, M., Arranz Yagüe, E., Pocoví, A., Galé Bornao, C., & Gil-Imaz, A. (2004). Lower Permian magmatism of the Iberian Chain and its relationship to extensional tectonics. In M. Wilson, E. R. Neumann, G. Davies, M. Timmermann, M. Heeremans, & B. T. Larsen (Eds.) *Permo-Carboniferous magmatism and rifting in Europe* (Vol. 223, pp. 465–491). Special Publication, Geological Society of London. https://doi.org/10.1144/GSL.SP.2004.223.01.20

Lamolda, M., Mathey, B., Rossy, M., & Sigal, J. (1983). La edad del volcanismo cretácico de Vizcaya y Guipuzcoa. *Estudios Geologicos*, *39*, 151–156.

Larin, N., Zgonnik, V., Rodina, S., Deville, E., Prinzhofer, A., & Larin, V. N. (2015). Natural molecular hydrogen seepage associated with surficial, Rounded depressions on the European Craton in Russia. *Natural Resources Research*, *24*(3), 369–383. https://doi.org/10.1007/s11053-014-9257-5

Lefeuvre, N., Truche, L., Donzé, F.-V., Ducoux, M., Barré, G., Fakoury, R.-A., et al. (2021). Native H2 exploration in the western Pyrenean Foothills. *Geochemistry, Geophysics, Geosystems*, *22*(8), e2021GC009917. https://doi.org/10.1029/2021GC009917

Lefeuvre, N., Truche, L., Donzé, F.-V., Gal, F., Tremosa, J., Fakoury, R.-A., et al. (2022). Natural hydrogen migration along thrust faults in foothill basins: The North Pyrenean Frontal Thrust case study. *Applied Geochemistry*, *145*, 105396. https://doi.org/10.1016/j.apgeochem.2022.105396

Lehujeur, M., Chevrot, S., Villaseñor, A., Masini, E., Saspiturry, N., Lescoutre, R., & Sylvander, M. (2021). Three-dimensional shear velocity structure of the Mauléon and Arzacq basins (western Pyrenees). *BSGF Earth Sciences Bulletin*, *192*(1), 47. https://doi.org/10.1051/bsgf/2021039

Le Maire, P., Thinon, I., Tugend, J., Issautier, B., Martelet, G., Paquet, F., et al. (2021). New Magnetic compilation and interpretation of the Bay of Biscay and surrounding continental shelves. *BSGF Earth Sciences Bulletin*, *192*, 58. https://doi.org/10.1051/bsgf/2021048

Lescoutre, R., & Manatschal, G. (2020). Role of rift-inheritance and segmentation for orogenic evolution: Example from the Pyrenean-Cantabrian system. *BSGF - Earth Sciences Bulletin*, *191*(1), 18. https://doi.org/10.1051/bsgf/2020021

Lescoutre, R., Tugend, J., Brune, S., Masini, E., & Manatschal, G. (2019). Thermal evolution of Asymmetric hyperextended magma-poor rift systems: Results from Numerical modeling and Pyrenean field observations. *Geochemistry, Geophysics, Geosystems*, *20*(10), 4587. https://doi.org/10.1029/2019GC008600

Li, Z. Y., Zheng, J. P., Moskowitz, B. M., Liu, Q. S., Xiong, Q., Yang, J. S., & Hu, X. Y. (2017). Magnetic properties of serpentinized peridotites from the Dongbo ophiolite, SW Tibet: Implications for suture-zone magnetic anomalies. *Journal of Geophysical Research: Solid Earth*, *122*(7), 4814–4830. https://doi.org/10.1002/2017JB014241

Liu, Z., Perez-Gussinye, M., García-Pintado, J., Mezri, L., & Bach, W. (2023). Mantle serpentinization and associated hydrogen flux at North Atlantic magma-poor rifted margins. *Geology*, *51*(3), 284–289. https://doi.org/10.1130/G50722.1

Lloret, J. A., Ronchi, J., López-Gómez, N., Gretter, R., De la Horra, J. F., Barrenechea, A., & Arche, A. (2018). Syn-tectonic sedimentary evolution of the continental late Palaeozoic-early Mesozoic Erill Castell-Estac basin and its significance in the development of the central Pyrenees basin. *Sedimentary Geology*, *374*, 134–157. https://doi.org/10.1016/j.sedgeo.2018.07.014

Loiseau, K., Aubourg, C., Petit, P., Bordes, S., Lefeuvre, N., Thomas, E., et al. (2024). H2 generation and heterogeneity of the serpentinization process at all scales: Turon de Técouère lherzolite case study, Pyrenees (France). *Geoenergy*, *2*(1), geoenergy2023024. https://doi.org/10.1144/geoenergy2023-024

López-Horgue, M. A., Owen, H. G., Rodríguez-Lázaro, J., Fernández-Mendiola, P. A., García-Mondéjar, J., & García-Mondéjar, J. (1999). Late Albian–Early Cenomanian stratigraphic succession near Estella-Lizarra (Navarra, central northern Spain) and its regional and interregional correlation. *Cretaceous Research*, *20*(4), 369–402. https://doi.org/10.1006/cres.1999.0162

Lucas, C. (1985). Le grès rouge du versant nord des Pyrénées: essai sur la géodynamique de dépôts continentaux du permien et du trias (p. 267).

Maffione, M., Morris, A., Plümper, O., & van Hinsbergen, D. J. J. (2014). Magnetic properties of variably serpentinized peridotites and their implication for the evolution of oceanic core complexes. *Geochemistry, Geophysics, Geosystems*, *15*(4), 923–944. https://doi.org/10.1002/2013GC004993

Malvoisin, B., Brantut, N., & Kaczmarek, M.-A. (2017). Control of serpentinisation rate by reaction-induced cracking. *Earth and Planetary Science Letters*, *476*, 143–152. https://doi.org/10.1016/j.epsl.2017.07.042

Manatschal, G. (2004). New models for evolution of magma-poor rifted margins based on a review of data and concepts from West Iberia and the Alps. *International Journal of Earth Sciences*, *93*(3), 432–466.

Manatschal, G., Engström, A., Desmurs, L., Schaltegger, U., Cosca, M., Müntener, O., & Bernoulli, D. (2006). What is the tectono-metamorphic evolution of continental break-up: The example of the Tasna Ocean–Continent transition. *Journal of Structural Geology*, *28*(10), 1849–1869. https://doi.org/10.1016/j.jsg.2006.07.014

Marcaillou, C., Muñoz, M., Vidal, O., Parra, T., & Harfouche, M. (2011). Mineralogical evidence for H2 degassing during serpentinization at 300°C/300bar. *Earth and Planetary Science Letters*, *303*(3), 281–290. https://doi.org/10.1016/j.epsl.2011.01.006

Martelet, G., Debéglia, N., & Truffert, C. (2002). Homogénéisation et validation des corrections de terrain gravimétriques jusqu'à la distance de 167 km sur l'ensemble de la France. *Comptes Rendus Geoscience*, *334*(7), 449–454. https://doi.org/10.1016/S1631-0713(02)01779-0

Martelet, G., Pajot, G., & Debeglia, N. (2009). Nouvelle carte gravimétrique de la France; RCGF09—Réseau et Carte Gravimétrique de la France (No. BRGM/RP-57908-FR) (p. 77).

Martin, R., Chevrot, S., Komatitsch, D., Seoane, L., Spangenberg, H., Wang, Y., et al. (2017). A high-order 3-D spectral-element method for the forward modelling and inversion of gravimetric data—Application to the western Pyrenees. *Geophysical Journal International*, *209*(1), 406–424. https://doi.org/10.1093/gji/ggx010

Masini, E., Manatschal, G., Tugend, J., Mohn, G., & Flament, J.-M. (2014). The tectono-sedimentary evolution of a hyper-extended rift basin: The example of the Arzacq–Mauléon rift system (western Pyrenees, SW France). *International Journal of Earth Sciences*, *103*(6), 1569–1596. https://doi.org/10.1007/s00531-014-1023-8

McCollom, T. M., & Bach, W. (2009). Thermodynamic constraints on hydrogen generation during serpentinization of ultramafic rocks. *Geochimica et Cosmochimica Acta*, *73*(3), 856–875. https://doi.org/10.1016/j.gca.2008.10.032

McCollom, T. M., Klein, F., Robbins, M., Moskowitz, B., Berquó, T. S., Jöns, N., et al. (2016). Temperature trends for reaction rates, hydrogen generation, and partitioning of iron during experimental serpentinization of olivine. *Geochimica et Cosmochimica Acta*, *181*, 175–200. https://doi.org/10.1016/j.gca.2016.03.002

McCollom, T. M., & Shock, E. L. (1997). Geochemical constraints on chemolithoautotrophic metabolism by microorganisms in seafloor hydrothermal systems. *Geochimica et Cosmochimica Acta*, *61*(20), 4375–4391. https://doi.org/10.1016/S0016-7037(97)00241-X

Miller, D. J., & Christensen, N. I. (1997). Seismic velocities of lower crustal and upper mantle rocks from the slow-spreading Mid-Atlantic Ridge, south of the Kane Fracture Zone (MARK). *Proceedings of the Ocean Drilling Program, Scientific Results*, 437–454.

Montigny, R., Azambre, B., Rossy, M., & Thuizat, R. (1986). K-Ar study of Cretaceous magmatism and metamorphism in the Pyrenees: Age and length of rotation of the Iberian Peninsula. *Tectonophysics*, *129*(1–4), 257–273. https://doi.org/10.1016/0040-1951(86)90255-6

Moretti, I., Prinzhofer, A., Françolin, J., Pacheco, C., Rosanne, M., Rupin, F., & Mertens, J. (2021). Long-term monitoring of natural hydrogen superficial emissions in a brazilian cratonic environment. Sporadic large pulses versus daily periodic emissions. *International Journal of Hydrogen Energy*, *46*(5), 3615–3628. https://doi.org/10.1016/j.ijhydene.2020.11.026

Muñoz, J. A. (1992). Evolution of a continental collision belt: ECORS-pyrenees crustal balanced cross-section. In K. R. McClay (Ed.), *Thrust tectonics* (pp. 235–246). Springer Netherlands. https://doi.org/10.1007/978-94-011-3066-0_21

Nazarova, K. A. (1994). Serpentinized peridotites as a possible source for oceanic magnetic anomalies. *Marine Geophysical Researches*, *16*(6), 455–462. https://doi.org/10.1007/bf01270519

Neal, C., & Stanger, G. (1983). Hydrogen generation from mantle source rocks in Oman. *Earth and Planetary Science Letters*, *66*, 315–320. https://doi.org/10.1016/0012-821X(83)90144-9

Neres, M., Bouchez, J., Terrinha, P., Font, E., Moreira, M., Miranda, R., et al. (2014). Magnetic fabric in a Cretaceous sill (Foz da Fonte, Portugal): Flow model and implications for regional magmatism. *Geophysical Journal International*, *199*(1), 78–101. https://doi.org/10.1093/gji/ggu250

Neres, M., Font, E., Miranda, J., Camps, P., Terrinha, P., & Mirão, J. (2012). Reconciling cretaceous paleomagnetic and marine magnetic data for Iberia: New Iberian paleomagnetic poles. *Journal of Geophysical Research*, *117*(B6), B06102. https://doi.org/10.1029/2011JB009067

Neres, M., Terrinha, P., Custódio, S., Silva, S. M., Luis, J., & Miranda, J. M. (2018). Geophysical evidence for a magmatic intrusion in the ocean-continent transition of the SW Iberia margin. *Tectonophysics*, *744*, 118–133. https://doi.org/10.1016/j.tecto.2018.06.014

Olivet, J. L. (1996). La cinématique de la plaque ibérique. *Bulletin Centre Recherche Exploration Production Elf Aquitaine*, *20*, 131–195.

Oufi, O., Cannat, M., & Horen, H. (2002). Magnetic properties of variably serpentinized abyssal peridotites. *Journal of Geophysical Research*, *107*(5), EPM3-1–EPM3-20. https://doi.org/10.1029/2001JB000549

Pedreira, D., Pulgar, J. A., Gallart, J., & Torné, M. (2007). Three-dimensional gravity and magnetic modeling of crustal indentation and wedging in the western Pyrenees-Cantabrian Mountains. *Journal of Geophysical Research*, *112*(B12), 30167. https://doi.org/10.1029/2007JB005021

Pedrera, A., García-Senz, J., Ayala, C., Ruiz-Constán, A., Rodríguez-Fernández, L. R., Robador, A., & González Menéndez, L. (2017). Reconstruction of the exhumed mantle across the North Iberian margin by crustal-scale 3-D gravity inversion and geological cross section: Mantle along the Basque-Cantabrian basin. *Tectonics*, *36*(12), 3155–3177. https://doi.org/10.1002/2017TC004716

Pedrera, A., Ruiz-Constán, A., García-Senz, J., Azor, A., Marín-Lechado, C., Ayala, C., et al. (2020). Evolution of the South-Iberian paleomargin: From hyperextension to continental subduction. *Journal of Structural Geology*, *138*, 104122. https://doi.org/10.1016/j.jsg.2020.104122

Prinzhofer, A., Moretti, I., Françolin, J., Pacheco, C., D'Agostino, A., Werly, J., & Rupin, F. (2019). Natural hydrogen continuous emission from sedimentary basins: The example of a Brazilian H2-emitting structure. *International Journal of Hydrogen Energy*, *44*(12), 5676–5685. https://doi.org/10.1016/j.ijhydene.2019.01.119

Prinzhofer, A., Tahara Cissé, C. S., & Diallo, A. B. (2018). Discovery of a large accumulation of natural hydrogen in Bourakebougou (Mali). *International Journal of Hydrogen Energy*, *43*(42), 19315–19326. https://doi.org/10.1016/j.ijhydene.2018.08.193

Pueyo, E., Izquierdo-Llavall, E., Rodríguez-Pintó, A., Rey-Moral, C., Oliva-Urcia, B., Casas-Sainz, A., et al. (2015). Petrophysical properties in the Iberian range and surrounding areas (NE Spain): 1-density. *Journal of Maps*, *12*(5), 1–9. https://doi.org/10.1080/17445647.2015.1084545

Puigdefàbregas, C., & Souquet, P. (1986). Tecto-sedimentary cycles and depositional sequences of the Mesozoic and Tertiary from the Pyrenees. *Tectonophysics*, *129*(1–4), 173–203. https://doi.org/10.1016/0040-1951(86)90251-9

Rat, P. (1959). *Les pays crétacés: Basco-cantabriques (Espagne)*. Presses universitaires de France.

Rat, P., Amiot, M., Feuillée, P., Floquet, M., Mathey, B., Pascal, A., et al. (1983). Vue sur le Cretacé basco-cantabrique et nord-ibérique. Une Marge Son Arrière-Pays Ses Environ. Sedimentaires. *Mémoires géologiques de l'Université de Dijon*, *9*, 191.

Ribeiro, P., Silva, P., Moita, P., Kratinova, Z., Marques, F., & Henry, B. (2013). Palaeomagnetism in the Sines massif (SW Iberia) revisited: Evidences for late cretaceous hydrothermal alteration and associated partial remagnetization. *Geophysical Journal International*, *195*(1), 176–191. https://doi.org/10.1093/gji/ggt261

Rigo, A., Vernant, P., Feigl, K. L., Goula, X., Khazaradze, G., Talaya, J., et al. (2015). Present-day deformation of the Pyrenees revealed by GPS surveying and earthquake focal mechanisms until 2011. *Geophysical Journal International*, *201*(2), 947–964. https://doi.org/10.1093/gji/ggv052

Rodríguez-Méndez, L. J., Cuevas, J. J., Esteban, J. M., Tubía, S., Sergeev, S., & Larionov, A. (2014). Age of the magmatism related to the inverted Stephanian–Permian basin of the Sallent area (Pyrenees). *Geological Society, London, Special Publications*, *394*(1), 101–111. https://doi.org/10.1144/SP394.2

Roma, M., Ferrer, O., Roca, E., Pla, O., Escosa, F. O., & Butillé, M. (2018). Formation and inversion of salt-detached ramp-syncline basins. Results from analog modeling and application to the Columbrets Basin (Western Mediterranean). *Tectonophysics*, *745*, 214–228. https://doi.org/10.1016/j.tecto.2018.08.012

Rosenbaum, G., Lister, G. S., & Duboz, C. (2002). Relative motions of Africa, Iberia and Europe during Alpine orogeny. *Tectonophysics*, *359*(1–2), 117–129. https://doi.org/10.1016/S0040-1951(02)00442-0

Rossi, P., Cocherie, A., Fanning, C. M., & Ternet, Y. (2003). Datation U-Pb sur zircons des dolérites tholéiitiques pyrénéennes (ophites) à la limite Trias–Jurassique et relations avec les tufs volcaniques dits « infra-liasiques » nord-pyrénéens. *Comptes Rendus Geoscience*, *335*(15), 1071–1080. https://doi.org/10.1016/j.crte.2003.09.011

Rossy, M., Azambre, B., & Albarède, F. (1992). REE and Sr/1bNd isotope geochemistry of the alkaline magmatism from the cretaceous North Pyrenean rift zone (France-Spain). *Chemical Geology*, *97*(1–2), 33–46. https://doi.org/10.1016/0009-2541(92)90134-Q

Roure, F., Choukroune, P., Berastegui, X., Munoz, J. A., Villien, A., Matheron, P., et al. (1989). ECORS deep seismic data and balanced cross-sections: Geometric constraints on the evolution of the Pyrenees. *Tectonics*, *8*(1), 41–50. https://doi.org/10.1029/TC008i001p00041

Roux, J.-C. (1983). *Recherches stratigraphiques et sédimentologiques sur les flyschs crétacés pyrénéens au sud d'Oloron (Pyrénées Atlantiques). PhD thesis* (p. 256). Université de Toulouse.

Sallarès, V., Martínez-Loriente, S., Prada, M., Gràcia, E., Ranero, C., Gutscher, M. A., et al. (2013). Seismic evidence of exhumed mantle rock basement at the Gorringe Bank and the adjacent Horseshoe and Tagus abyssal plains (SW Iberia). *Earth and Planetary Science Letters*, *365*, 120–131. https://doi.org/10.1016/j.epsl.2013.01.021

Saspiturry, N., Allanic, C., & Peyrefitte, A. (2024). Dataset of joint gravimetric and magnetic forward 2D modelling of the Mauléon basin (Pyrenees) [Dataset]. *Mendeley Data, V1*. https://doi.org/10.17632/kmh5mr4dvp.1

Saspiturry, N., Allanic, C., Razin, P., Issautier, B., Baudin, T., Lasseur, E., et al. (2020). Closure of a hyperextended system in an orogenic lithospheric pop-up, Western Pyrenees: The role of mantle buttressing and rift structural inheritance. *Terra Nova*, *32*(4), 253–260. https://doi.org/10.1111/ter.12457

Saspiturry, N., Allanic, C., Serrano, O., Courrioux, G., Baudin, T., Le Bayon, B., et al. (2022). Upper lithospheric transfer zones driving the non-cylindricity of the West-Pyrenean orogenic prism (Mauléon hyperextended basin). *Journal of Structural Geology*, *156*, 104535. https://doi.org/10.1016/j.jsg.2022.104535

Saspiturry, N., Cochelin, B., Razin, P., Leleu, S., Lemirre, B., Bouscary, C., et al. (2019). Tectono-sedimentary evolution of a rift system controlled by Permian post-orogenic extension and metamorphic core complex formation (Bidarray Basin and Ursuya dome, Western Pyrenees). *Tectonophysics*, *768*, 228180. https://doi.org/10.1016/j.tecto.2019.228180

Saspiturry, N., Issautier, B., Razin, P., Andrieu, S., Lasseur, E., Allanic, C., et al. (2021). Review of the syn-rift to early post-rift depositional systems of the cretaceous Mauléon rift: Sedimentary record of continental crust hyperextension and mantle denudation (western Pyrenees). *BSGF - Earth Sciences Bulletin*, *192*, 49. https://doi.org/10.1051/bsgf/2021044

Saspiturry, N., Issautier, B., Razin, P., Baudin, T., Asti, R., Lagabrielle, Y., et al. (2021). Review of Iberia-Eurasia plate-boundary basins: Role of sedimentary burial on depth-dependent continental crust ductile thinning during rifting and continental breakup. *Basin Research*, *33*(2), 1626–1661. https://doi.org/10.1111/bre.12529

Saspiturry, N., Lahfid, A., Baudin, T., Guillou-Frottier, L., Razin, P., Issautier, B., et al. (2020). Paleogeothermal gradients across an inverted hyperextended rift system: Example of the Mauléon fossil rift (western Pyrenees). *Tectonics*, *39*(10), e2020TC006206. https://doi.org/10.1029/2020TC006206

Saspiturry, N., Razin, P., Baudin, T., Serrano, O., Issautier, B., Lasseur, E., et al. (2019). Symmetry vs. asymmetry of a hyper-thinned rift: Example of the Mauléon Basin (western Pyrenees, France). *Marine and Petroleum Geology*, *104*, 86–105. https://doi.org/10.1016/j.marpetgeo.2019.03.031

Schoeffler, J., Henry, J., & Villanova, M. (1964). État des travaux de cartographie géologique réalisés par la Société Nationale des Pétroles d'Aquitaine (SNPA) dans les Pyrénées occidentales. *Compte Rendu Sommaire des Seances de la Societe Geologique de France*, *7*, 241–246.

Schwartz, E., & Friedrich, B. (2006). The H2-metabolizing prokaryotes. *The Prokaryotes*, *7*, 496–563. https://doi.org/10.1007/0-387-30742-7_17

Serrano, O., Delmas, J., Hanot, F., Vially, R., Herbin, J.-P., Houel, P., & Tourlière, B. (2006). *Le bassin d'Aquitaine: valorisation des données sismiques, cartographie structurale et potentiel pétrolier* (p. 245). Bureau de Recherche Géologique et minière.

Souriau, A., & Pauchet, H. (1998). A new synthesis of Pyrenean seismicity and its tectonic implications. *Tectonophysics*, *290*(3–4), 221–244. https://doi.org/10.1016/S0040-1951(98)00017-1

Sylvander, M., Rigo, A., Sénéchal, G., Battaglia, J., Benahmed, S., Calvet, M., et al. (2021). Seismicity patterns in southwestern France. *Comptes Rendus Geoscience*, *353*(S1), 79–104. https://doi.org/10.5802/crgeos.60

Teixell, A., Labaume, P., & Lagabrielle, Y. (2016). The crustal evolution of the west-central Pyrenees revisited: Inferences from a new kinematic scenario. *Comptes Rendus Geoscience*, *348*(3), 257–267. https://doi.org/10.1016/j.crte.2015.10.010

Thiébaut, J., Debeaux, M., Debroas, E. J., & Souquet, P. (1979). Découverte de roches d'affinités teschenitiques dans les marbres mésozoïques de Saint-Béat (Haute-Garonne). *Comptes Rendus de l'Académie des Sciences*, *288*, 1695–1697.

Thinon, I., Matias, L., Réhault, J. P., Hirn, A., Fidalgo-GonzÁlez, L., & Avedik, F. (2003). Deep structure of the Armorican basin (bay of biscay): A review of Norgasis seismic reflection and refraction data. *Journal of the Geological Society*, *160*(1), 99–116. https://doi.org/10.1144/0016-764901-103

Tichadou, C., Godard, M., Munoz, M., Labaume, P., Vauchez, A., Gaucher, E., & Calassou, S. (2021). Mineralogical and geochemical study of serpentinized peridotites from the north-western Pyrenees: New insights on serpentinization along magma-poor continental passive margins. *Lithos*, *406*, 106521. https://doi.org/10.1016/j.lithos.2021.106521

Toft, P. B., Arkani-Hamed, J., & Haggerty, S. E. (1990). The effects of serpentinization on density and magnetic susceptibility: A petrophysical model. *Physics of the Earth and Planetary Interiors*, *65*(1), 137–157. https://doi.org/10.1016/0031-9201(90)90082-9

Torné, M., De Cabissole, B., Bayer, R., Casas, A., Daignières, M., & Rivero, A. (1989). Gravity constraints on the deep structure of the Pyrenean belt along the ECORS profile. *Tectonophysics*, *165*(1), 105–116. https://doi.org/10.1016/0040-1951(89)90039-5

Truche, L., Berger, G., Destrigneville, C., Guillaume, D., & Giffaut, E. (2010). Kinetics of pyrite to pyrrhotite reduction by hydrogen in calcite buffered solutions between 90 and 180°C: Implications for nuclear waste disposal. *Geochimica et Cosmochimica Acta*, *74*(10), 2894–2914. https://doi.org/10.1016/j.gca.2010.02.027

Truche, L., Berger, G., Destrigneville, C., Pages, A., Guillaume, D., Giffaut, E., & Jacquot, E. (2009). Experimental reduction of aqueous sulphate by hydrogen under hydrothermal conditions: Implication for the nuclear waste storage. *Geochimica et Cosmochimica Acta*, *73*(16), 4824–4835. https://doi.org/10.1016/j.gca.2009.05.043

Truche, L., McCollom, T. M., & Martinez, I. (2020). Hydrogen and abiotic Hydrocarbons: Molecules that change the world. *Elements*, *16*(1), 13–18. https://doi.org/10.2138/gselements.16.1.13

Tugend, J., Manatschal, G., Kusznir, N. J., Masini, E., Mohn, G., & Thinon, I. (2014). Formation and deformation of hyperextended rift systems: Insights from rift domain mapping in the Bay of Biscay-Pyrenees. *Tectonics*, *33*(7), 1239–1276. https://doi.org/10.1002/2014TC003529

Vacher, P., & Souriau, A. (2001). A three-dimensional model of the Pyrenean deep structure based on gravity modelling, seismic images and petrological constraints. *Geophysical Journal International*, *145*(2), 460–470. https://doi.org/10.1046/j.0956-540x.2001.01393.x

Wang, Y., Chevrot, S., Monteiller, V., Komatitsch, D., Mouthereau, F., Manatschal, G., et al. (2016). The deep roots of the western Pyrenees revealed by full waveform inversion of teleseismic P waves. *Geology*, *44*(6), 475–478. https://doi.org/10.1130/G37812.1

Wehr, H., Chevrot, S., Courrioux, G., & Guillen, A. (2018). A three-dimensional model of the Pyrenees and their foreland basins from geological and gravimetric data. *Tectonophysics*, *734*, 16–32. https://doi.org/10.1016/j.tecto.2018.03.017

Welhan, J. A., & Craig, H. (1979). Methane and hydrogen in east Pacific Rise hydrothermal fluids. *Geophysical Research Letters*, *6*(11), 829–831. https://doi.org/10.1029/GL006i011p00829

Zgonnik, V., Beaumont, V., Deville, E., Larin, N., Pillot, D., & Farrell, K. M. (2015). Evidence for natural molecular hydrogen seepage associated with Carolina bays (surficial, ovoid depressions on the Atlantic Coastal Plain, Province of the USA). *Progress in Earth and Planetary Science*, *2*(1), 31. https://doi.org/10.1186/s40645-015-0062-5